Review Vol. 30, No. 5 / 28 Feb 2022 / Optics Express 7253
Optics EXPRESS

Advances in integrated ultra-wideband electro-optic modulators [Invited]

MENGYUE XU AND XINLUN CAI*

State Key Laboratory of Optoelectronic Materials and Technologies and School of Electronics and Information Technology, Sun Yat-sen University, Guangzhou 510000, China
*caixlun5@mail.sysu.edu.cn

Abstract: Increasing data traffic and bandwidth-hungry applications require electro-optic modulators with ultra-wide modulation bandwidth for cost-efficient optical networks. Thus far, integrated solutions have emerged to provide high bandwidth and low energy consumption in compact sizes. Here, we review the design guidelines and delicate structures for higher bandwidth, applying them to lumped-element and traveling-wave electrodes. Additionally, we focus on candidate material platforms with the potential for ultra-wideband optical systems. By comparing the superiority and mechanism limitations of different integrated modulators, we design a future roadmap based on the recent advances.

1. Introduction

Network traffic is increasing at an alarming speed, largely driven by bandwidth-hungry applications such as 5G networks, Internet-to-Things (IoT) devices, video streaming, and cloud-based services [1]. To meet the ever-growing demand, cost-efficient optical networks are required for supporting high-speed optical links. High-performance electro-optic modulators are the critical building blocks in high-speed optical links, and they encode high-speed electrical information into an optical carrier with high fidelity. To enable cost-efficient and high-speed optical links, efforts are made to minimize the number of electro-optic (EO) interfaces of parallel lanes, and this is where high-symbol-rate transmission occurs. Under this scenario, a single optical modulator is used to encode high-symbol-rate electrical signals into an optical carrier. Therefore, the bandwidth of future EO modulators plays a crucial role and is expected to exceed 100 GHz. Meanwhile, a small footprint and low driving voltage of the EO modulators are necessary to match the CMOS electronic driving circuitry.

The bandwidth of the modulator is strongly related to the design of the driving electrodes of the modulator devices and the EO modulation mechanism of the underlying material. The EO modulator is typically classified into two types based on the configuration of the modulated electrode: lumped elements and traveling-wave modulators. The lumped-element device typically adopts short lumped electrodes (LEs) in optical resonators or slow-light waveguides for efficient modulation. The premise of a large bandwidth of greater than 100 GHz for most of the LE modulator is that the length of the electrode should be less than 500 µm, which is impractical for achieving efficient modulation for most EO materials. To achieve low drive voltages and high modulation bandwidth simultaneously, EO modulators with traveling-wave electrodes (TWEs) are a better choice [2–4]. In the TWE configuration, microwaves and optical waves propagate at a similar velocity, allowing the EO-induced refractive index changes to accumulate effectively in the optical waveguide. The challenges of a large modulation bandwidth are how to decrease microwave attenuation and how to realize velocity and impedance matching [5,6]. The design and optimization methodology of TWE modulators are different for different material platforms.

This review aims to provide a comprehensive review of various EO modulators that provide an ultra-wide bandwidth. From the scheme level viewpoint, we discuss the design considerations for the LE and TWE modulators. Novel configurations and techniques that can broaden the

#449022 https://doi.org/10.1364/OE.449022
Journal © 2022 Received 21 Nov 2021; revised 25 Jan 2022; accepted 29 Jan 2022; published 17 Feb 2022

Optics EXPRESS

modulation bandwidth are summarized in brief design guidelines. We also summarize the state-of-the-art modulators on various material platforms that are promising or have attained an EO bandwidth beyond 100 GHz, covering lithium niobate on insulator (LNOI), InP, SOI, and hybrid Si (silicon-organic hybrid, plasmonic-organic hybrid, LN/Si, GeSi). Finally, we compare the pros and cons of these modulators and provide a future outlook of promising candidates for EO modulators in ultra-wideband systems.

2. Paths toward higher modulation bandwidth

2.1. Lumped-element modulator

In the lumped element modulator, the RC constant of the electrode and the photon lifetime of the resonator together limit the overall EO bandwidth. Typically, the length of the LE is designed according to the following criterion [3]

$$l_{LE} < \frac{\lambda_{RF}}{10 n_{RF}} \tag{1}$$

where λ_{RF} is the RF wavelength and n_{RF} is the RF effective index. For a moderate RC-limited bandwidth, the length of the LE must be relatively short (typically < 500 μm). However, short phase shifters usually result in low modulation efficiency unless resonant cavities or slow-light structures are employed.

Resonant structures were introduced into LE-based modulators for effective modulation. The reported optical implementation includes micro-rings [7–12], racetracks [13–15], microdisk [16], Fabry–Perot (FP) cavity [17], and photonic crystal (PhC) structure [18–20] (Fig. 1). The advanced silicon micro-ring modulator showed a high tuning efficiency of 33 pm/V and a data rate of 160 Gbit/s [11]. An ultra-high tuning efficiency of 250 pm/V had been realized in a microdisk silicon modulator with the optimized vertical junction [16]. An integrated FP modulator was demonstrated on the LNOI platform, where the FP cavity comprises an 800-μm phase shifter sandwiched between two distributed Bragg reflectors (DBR) [17]. PhC waveguides can offer a slow-light effect and strong EO interaction [18–20] and PhC-based LN modulators [18] demonstrate low energy consumption (< 2 fJ/bit) for a 50 Gbit/s eye diagram (Figs. 2(a) and (b)). In the aforementioned resonant modulators, most of the 3-dB EO bandwidth does not exceed 40 GHz, which is dominantly limited by photon lifetime owing to relatively high quality (Q) factor. The EO bandwidth can reach 47 GHz by reducing the Q factor to ~3000 [11]. Furthermore, the RC bandwidth is predicted to achieve a 90-GHz bandwidth attribute of the small device capacitance [12]. Hence, for the resonant modulator, it is essential to balance the modulation efficiency and EO bandwidth, which are both related to the Q factor.

A non-resonant LE-based modulator can overcome the limit of the photon lifetime. However, longer LEs are usually required to achieve low drive voltages and deteriorate the RC bandwidth. A promising solution that might break the trade-off is to employ a Bragg reflector [21] or plasmonic waveguides [22]. As shown in Figs. 2(c) and (d), the 420-μm-long LNOI modulator based on waveguide Bragg grating displays an EO bandwidth of 60 GHz and 100 Gbaud on-off keying (OOK) modulation [21]. Plasmonic organic hybrid (POH) modulators offer tight optical and microwave confinement in a narrow metal slot waveguide (~100 nm). The strong EO interaction and the high EO coefficient of the organic materials filled in the slot enable the POH modulator to achieve low drive voltages of tens of microns. As shown in Fig. 2(e), the 20-μm-long POH modulator exhibited an ultra-high modulation bandwidth of 500 GHz and half-wave voltage (V_π) of 3 V [22].

2.2. Traveling-wave modulator

The keys to achieve ultra-wide modulation bandwidth in the travelling-wave scheme are: (a) low microwave propagation loss, (b) propagation speed matching between optical waves and

Optics EXPRESS

microwaves, and (c) impedance matching among the modulator, the electrical system, and the terminator.

Microwave propagation loss (α_{RF}) degrades the modulation bandwidth, especially for modulators requiring long TWEs. To reduce the α_{RF} of CPW, we investigated the attenuations primarily from the following parameters [23]:

$$\alpha = \alpha_c + \alpha_d \tag{2}$$

where α_c and α_d are the conductor and dielectric losses, respectively. α_d is the frequency (f) dependent and can be expressed as [24]:

$$\alpha_d = \frac{\pi}{\lambda_0}\frac{\varepsilon_r}{\sqrt{\varepsilon_{eff}}} q \tan\delta \tag{3}$$

where λ_0 is the free space wavelength, ε_{eff} is the effective dielectric constant, and q is the filling factor. $tan\delta$ includes the total tangent from lossy dielectric media, which is composed of the material intrinsic loss ($tan\delta_D$) and the substrate leakage loss ($tan\delta_L$). The dielectric has the complex permittivity $\varepsilon = \varepsilon' - j\varepsilon''$. $tan\delta_D$ is related only to the complex dielectric permittivity of the materials. $tan\delta_L$ is dependent on the frequency and is proportional to the conductivity (σ) of the substrate [25]:

$$\tan\delta = \tan\delta_D + \tan\delta_L \tag{4}$$

$$\tan\delta_D = \frac{\varepsilon''}{\varepsilon'} \tag{5}$$

$$\tan\delta_L = \frac{\sigma}{2\pi f \varepsilon'} \tag{6}$$

Considering a modulator based on the LNOI platform with a silicon substrate as an example, the resistivity of the silicon substrate needs to be large enough (~ 10000 Ωcm) to minimize $tan\delta_L$. Replacing the silicon substrate ($tan\delta_D$ =0.043 [25]) with quartz ($tan\delta_D$~ 10^{-5} [26]), sapphire ($tan\delta_D$ ~10^{-7} [27]), or other materials with low $tan\delta_D$ can effectively reduce the dielectric loss. As shown in Figs. 3(a) and (b), Li et al. [28] successfully achieved EO bandwidth exceeding 50 GHz by removing the silicon substrate around the TWE in a silicon modulator. The improved bandwidth can be attributed to the replacement of high-$tan\delta_D$ silicon with air, resulting in lower dielectric losses.

Metal surface resistivity accounts for α_c, which is proportional to the square-root frequency ($\sqrt{f}$) when the electrode thickness is much larger than the skin depth. In principle, we can increase the thickness of the electrodes (1–2 μm), the width of the signal electrodes, and the gap between the signal and ground electrodes, to decrease α_c. However, these parameters also influence the

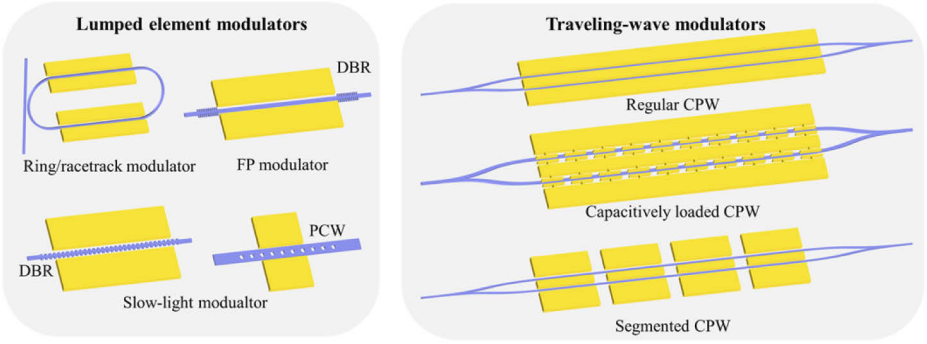

Fig. 1. Schematic illustration of several configurations with the lumped-element electrode and traveling-wave electrode performing amplitude modulation.

Optics EXPRESS

RF index and impedance value of the CPW, as well as the modulation efficiency. Therefore, we must carefully balance the trade-offs among α_c, velocity matching, impedance matching, and modulation efficiency. A delicate CPW scheme that can drastically reduce α_c without sacrificing velocity matching and modulation efficiency is the so-called capacitive-loaded CPW (CL-TWE) [29–31] (Fig. 1). The center conductor gap and width of the CL-TWEs are much larger than those of the regular CPW, resulting in less current crowding and a significant reduction in α_c. Moreover, the protruding periodic T-rails help ensure a high modulation efficiency. Most recently, LNOI-based modulators with low drive voltages and bandwidths beyond 100 GHz have been demonstrated with CL-TWEs and quartz substrates [32,33] (Figs. 3(c)-(e)).

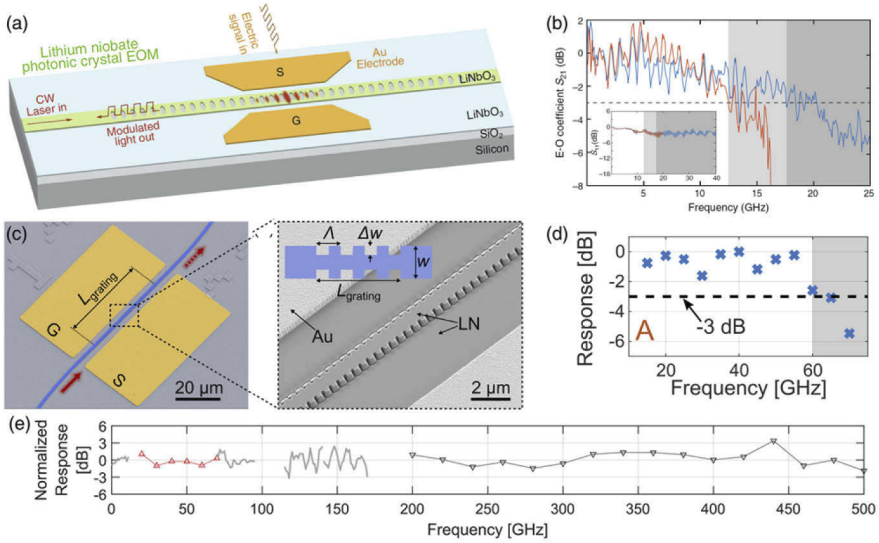

Fig. 2. (a-b) Schematic and measured EO S_{21} response of the PhC modulator [18], licensed under a Creative Commons Attribution 4.0 License. (c-d) SEM images and measured EO S_{21} response of Bragg grating modulator [21], licensed under a Creative Commons Attribution 4.0 License. (e) Measured EO S_{21} response of plasmonic organic hybrid modulator [22], licensed under a Creative Commons Attribution 4.0 License.

A promising alternative to increase the bandwidth of TW-based modulators is to split the modulation electrodes into two or more segments (Fig. 4) [34–37]. The modulators based on the segmented-electrode (SE) exhibit a higher modulation bandwidth than equivalent-length single-segment TWE. The velocity mismatch between microwave and light waves accumulates over length, however, the SE-MZM can return to matching by controlling the RF delays between segments. In [34], two-segment MZMs have experimentally shown better bandwidth/half-wave voltage (BW/V_π) performance than single-segment MZM. As the length of TWE increases, the voltage swing is significantly attenuated especially for high-frequency components, while SE-MZM with multi-segment short transmission lines means lower RF loss and lower driving voltage for each driver. However, more segments imply more electrical drivers, leading to additional power consumption and complexity from RF delay control among drivers. Recently, a silicon Mach-Zehnder modulator (MZM) with two SEs capable of transmitting 80 Gbaud 8-level pulse amplitude modulation (PAM8) over 2 km was presented [36] (Fig. 4(c)). In addition, both SE and CL-TWE are versatile across various material platforms, and the two technologies can be combined to further improve the EO modulation bandwidth.

Optics EXPRESS

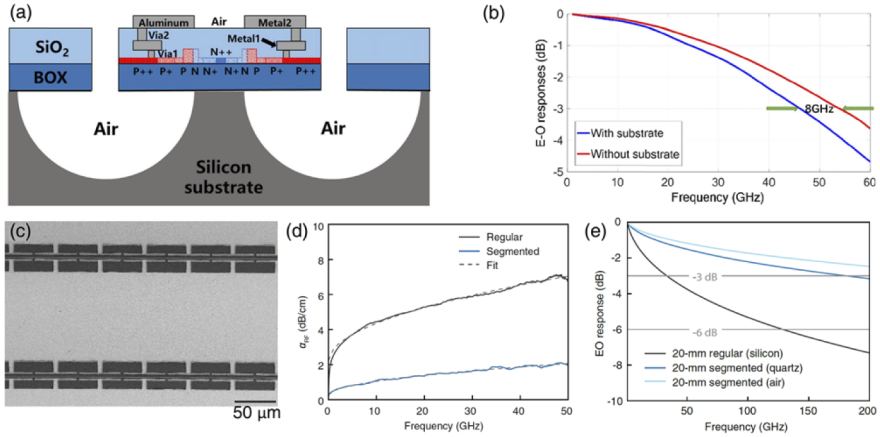

Fig. 3. (a-b) A cross-sectional diagram and the calculated EO S_{21} response of the silicon modulator using the substrate removing technique. Reprinted with permission from [28]. Copyright 2018, Chinese Laser Press. (c-e) SEM image, microwave loss of the CL-TWE and predicted EO S_{21} performance in thin-film LN-on-quartz platform. Reprinted with permission from [32]. Copyright 2021, Optical Society of America.

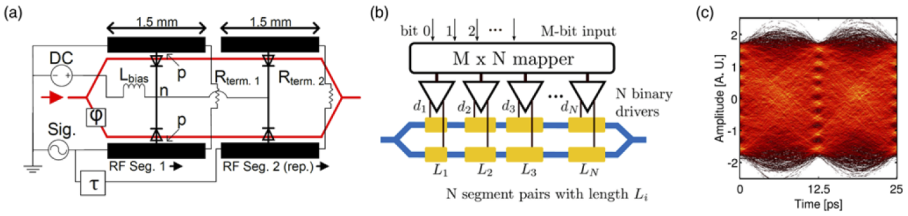

Fig. 4. (a) A two-segment modulator enabled by two drivers. Reprinted from M. Jacques et al. [35]. Copyright 2021, Author(s). (b) Distributed drivers with a *i*-segment modulator. Reprinted with permission from [38]. Copyright 2017, IEEE. (c) Generation of optical 80 Gbaud PAM8 with two-segment silicon modulator. Reprinted with permission from [36]. Copyright 2020, IEEE.

3. State-of-the-art of ultra-high-bandwidth modulators

3.1. *Thin-film LN modulator*

LN external modulators have been widely used in long-haul communication systems. The commercial LN modulator has achieved tremendous success mainly owing to its strong linear (Pockels) EO coefficient ($r_{33} = 30.8$ pm/V in high frequency) [39], large intrinsic bandwidth, and chirp-free operation. Furthermore, the low absorption loss (~0.17%/cm at 1.32 μm) [40] and the transparency range (0.4–5.5 μm) [41] contribute to its success. However, traditional LN modulators are based on ion-diffused or proton-exchange optical waveguides on bulk LN crystals [42]. Such weak-confined waveguides require electrodes to be placed away from them to achieve low metal absorption losses, and thus, low modulation efficiency (typical >10 Vcm). Therefore, traditional LN modulators require a long modulation region (at least 10 cm) to achieve a sub-1V V_π. Moreover, the EO bandwidth runs into a bottleneck (~35 GHz) owing to the high RF loss from the long electrodes.

The LNOI platform breaks the deadlock and takes the performance of the modulator to a new level. A critical step in improving the modulation performance is the fabrication of low-loss, highly-confined waveguides in LNOI. Thus, the electrodes can be placed very close to the edge of

Optics EXPRESS

the waveguides without introducing additional metal absorption losses. Therefore, the interaction between the electric and optical fields is significantly enhanced compared to the legacy LN modulator. Recently, researchers have demonstrated highly confined submicron waveguides by electron-beam lithography (EBL) [43–47] or photolithography [48,49] followed by dry-etching and mechanical polishing processes [50]. Extremely low optical losses of 6 dB/m (637 nm) [51] and 2.7 dB/m (1590 nm) [43] have been reported. Low-loss, high-speed, and energy-efficient travelling-wave LN modulators have been demonstrated by adopting patterned LN waveguide in the modulation region [44,52–57]. Alternative ways to form optical waveguides in LNOI platforms without patterning processes include rib-loaded waveguides [13,58–60], SOI-bonded [8,61], and SiN_x-bonded [62] waveguides. However, the mode confinement factor is limited to less than 81%, and it is difficult to further improve this factor. This results in a moderate modulation efficiency and a larger bending radius than the dry-etched LNOI devices.

A remarkable increase in bandwidth in the LNOI platform has been reported in the last three years [21,32,45,52,63–68]. Low-loss, energy-efficient, high-bandwidth LNOI-based modulators have shown ultra-high symbol rates and net rates both in intensity-modulated direct-detection (IM-DD) and coherent transmission systems. As shown in Fig. 5(a), V_π of 1.4V and EO bandwidth of 45 GHz were achieved simultaneously using an integrated MZM with regular CPW, according to a BW/V_π of 32 GHz/V [44], which significantly improved compared to the commercial LN (<10 GHz/V). With a similar device configuration, Yu et al. experimentally demonstrated a hard-decision forward error correction (HD-FEC) of 220 Gbit/s (110 Gbaud PAM-4) [55]. Advanced LN IQ modulators have been demonstrated in [52]. The device demonstrated the lowest on-chip loss (<1.8 dB) among the presented in-phase quadrature (IQ) modulators. The drive voltage was 1.9 V and the EO bandwidth was 48 GHz for a 13-mm device, and these values were 3.1 V and >67 GHz for a 7.5-mm device. Figure 5(b) shows 80 Gbaud error-free QPSK generation, 110 Gbaud QPSK generation, and 80 Gbaud 16 quadrature amplitude modulation (QAM) generation (320 Gbit/s) with a bit-error rate (BER) well below the soft-decision forward error correction (SD-FEC, 4×10^{-2}). Moreover, this work adopted thermo-optic phase shifters for bias control, avoiding the DC bias drifts in the EO phase shifter [70–72]. Recent achievements in the integrated LN modulators with CL-TWE again breach the voltage-bandwidth trade-off in the LN-on-quartz platform [32]. Importantly, the RF loss is measured to be as low as 0.21 dB/cm/$GHz^{1/2}$ without sacrificing the modulation efficiency. With the ultra-low RF loss and perfect velocity matching, a flat EO response (1.8 dB roll-off at 50 GHz) and V_π of 1.3 V was realized with a 20-mm-long modulator.

A record IM-DD modulation line rate of 700 Gb/s was achieved with an integrated LN MZM [57]. With regard to the dual-polarization coherent system, a net data rate of 1.58 Tb/s/λ was achieved with 200 Gbaud probabilistically shaped 64-QAM signal, which was enabled by a 100-GHz (6-dB bandwidth) LN IQ modulator, 102-GHz digital band interleaved-digital-to-analog converters (DBI-DACs), and a discrete polarization-division multiplexing (PDM) emulator [56]. Most recently, a LNOI-based dual-polarization in-phase quadrature (DP-IQ) integrated with an on-chip polarization rotator and combiner (PRC) has been demonstrated [69]. The device adopted the optimized 23.5-mm-long CL-TWEs for CMOS-level voltage and 110-GHz bandwidth. The high-performance device DP-IQ modulator allows for a record net bitrate of up to 1.96 Tb/s and ultra-low power consumption (1.04 fJ/bit) using a 130 Gbaud probabilistic constellation shaping (PCS-) 400QAM.

3.2. InP modulator

InP modulators have demonstrated superior performance in IM-DD [73–75] and coherent systems [76–78]. The EO effects in InP include the quantum-confined Stark effect (QCSE), Franz–Keldysh effect (FKE), and the Pockels effect, and these effects can be synergistic by

Optics EXPRESS

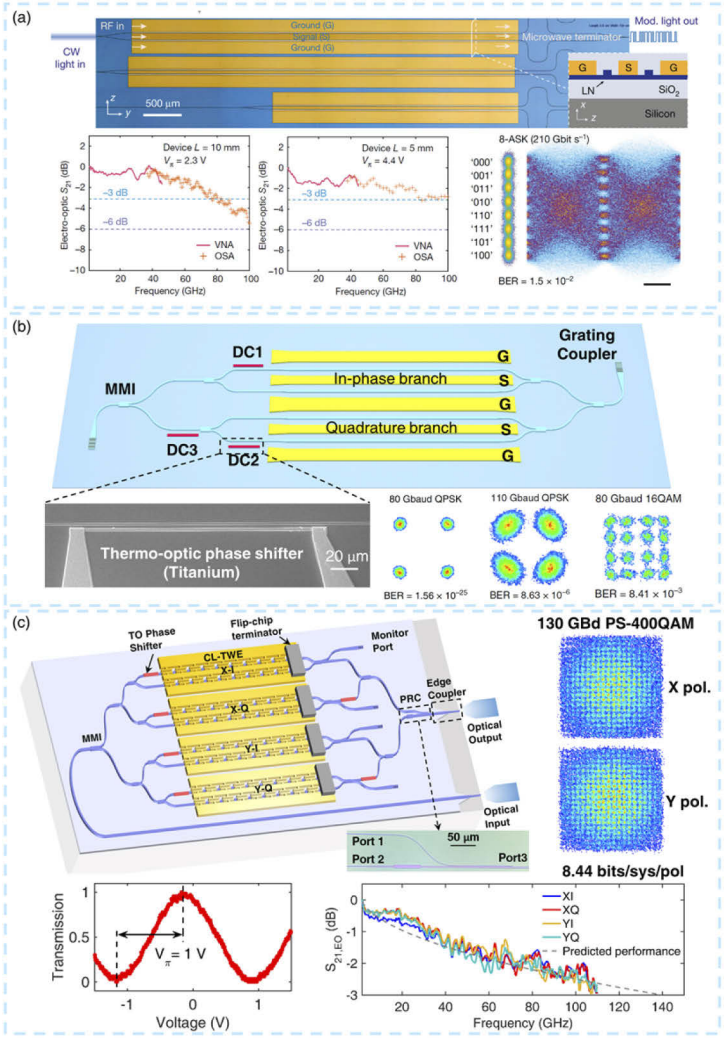

Fig. 5. High symbol rate modulations with LNOI-based modulators. (a) Intensity modulators with modulation up to 210 Gbit/s. Reprinted with permission from [36]. Copyright 2020, IEEE. (b) IQ modulators with modulation up to 320 Gbit/s [52], licensed under a Creative Commons Attribution 4.0 License. (c) CMOS-level-voltage and 110-GHz bandwidth DP-IQ modulator with and 130 Gbaud PS-400QAM. Reprinted with permission from [69]. Copyright 2022, Optica Publishing Group.

designing an optical waveguide structure [79]. The representative types of monolithic InP transceivers are electro-absorption modulated lasers (EMLs) and MZMs.

An InP-based EML typically consists of a monolithically integrated distributed feedback (DFB) laser and an electro-absorption modulator (EAM) [80,81]. A dominant EO effect of the EAMs is the QCSE, which provides intrinsic high bandwidth and strong nonlinear absorption in the InP-multiple quantum well (MQW) optical waveguides. The modulation length of the EAMs is of the order of hundreds of microns, which is highly related to the trade-off between the RC-limited bandwidth and the extinction ratio (ER). The DFB-EAM with segmented structure successfully overcame the RC limit, demonstrating a 100-GHz, 3-dB bandwidth [80] (see Fig. 6(a)) and 100 Gb/s operation [82].

Optics EXPRESS

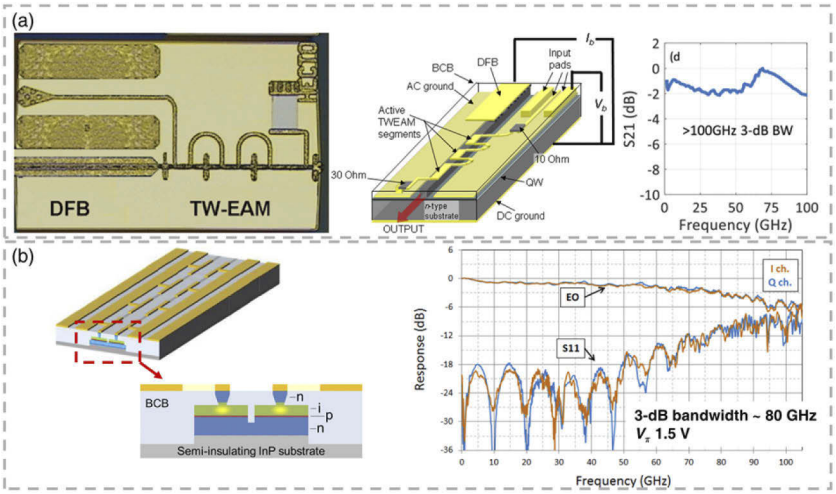

Fig. 6. (a) Monolithically electro-absorption modulated laser (EML). Reprinted with permission from [80]. Copyright 2009, IEEE. (b) High-performance InP-based CL-TWE modulators. Reprinted with permission from [77]. Copyright 2020, IEEE.

InP-based MZMs must optimize the heterostructure optical waveguide and TWE structure to balance the drive voltage, optical absorption loss, and modulation length. A conventional waveguide structure, p-doped/intrinsic/n-doped (p-i-n) structure in [0 $\bar{1}$ 1] direction [83], is replaced by a novel n-p-i-n structure, providing an increased bandwidth due to the low resistance of the p-InP cladding layer [84]. Ogiso et al. [85] first proposed an n-i-p-n heterostructure InP waveguide parallel to the [0 1 1] direction. The delicate heterostructure can provide lower RF losses, synergistic (FKE/QCSE and Pockels) EO effect, and low propagation optical loss (1.5 dB/cm). By employing this heterostructure, an InP-based MZM with 1.5-V V_π and 80-GHz EO bandwidth was demonstrated [77]. As shown in Fig. 6(b), the device adopts CL-TWE in the differential GSSG configuration to reduce high-frequency microwave loss and power consumption. The differential drive of the MZM leads to a close-to-zero chirp, which is superior to the EML and directly modulated laser (DML).

Furthermore, DAC-less modulation has been demonstrated with segmented electrode Mach-Zehnder Modulators (SEMZMs) in the InP platform (Fig. 4). This optical-DAC approach reduces the need for linearity and the voltage swing of each electrical driver. With 4-bit IQ SEMZMs, advanced modulation formats were presented in [86,87] with BiCMOS drivers, such as 32 Gbaud 256 QAM generation.

3.3. *Si and hybrid Si modulator*

Silicon photonics is preferred for its CMOS compatibility with microelectronics, dense nanophotonics integration, and low-cost mass production. High-speed all-silicon modulators typically rely on the plasma dispersion effect [88], which is modulated by changing the concentration of the PN junction free charge, leading to a change in the refractive index of the material, and ultimately changing the optical phase of the waveguides. The structure and design of the PN junction lead to a trade-off between efficiency and bandwidth, both of which are related to the junction capacitance. For a long time, all-silicon modulators featured limited bandwidth (< 45 GHz) and moderate V_π with modulation lengths of a few millimeters [31,89–92]. Some techniques have been used to increase the silicon MZM bandwidth, including removing the substrate (see Fig. 3) and terminating loads less than 50 Ω [93,94]. The peak effect occurs when

Optics EXPRESS

loads with lower terminators (~ 35 Ω) at a low frequency (~10 GHz) are used, which improves the bandwidth at the cost of suppressing the modulation depth at low frequencies.

In [95], the silicon MZM implemented two metal layers and a 35-Ω on-chip termination for lower microwave attenuation and higher EO bandwidth. The 47-GHz silicon MZM allows a net data rate of 225 Gbit/s at back-to-back transmission in the O-band. (Fig. 7(a)) In 2020, silicon MZMs demonstrated a 3-dB bandwidth of 60 GHz, adopting differential-driven CL-TWE and specific PN junction loading [96]. Furthermore, the high-bandwidth Si MZMs comprised four channels and were co-packaged with an electrical driver chip. The packaged transmitter demonstrated 800 Gbit/s (4×200 Gbit/s) PAM4 modulation on 3-V V_{pp} differential drives (Fig. 7(b)). The silicon microring modulator is much more compact and more power-efficient than the silicon MZM. Recently, a 3-dB-bandwidth greater than 67 GHz and 26.34-pm/V tuning efficiency silicon mirroring modulator was demonstrated [97]. As shown in Fig. 7(c), the EO response curve shows a peak at approximately 50 GHz, which is not limited by the photon lifetime (41 GHz). A 200 Gbit/s PAM4 was successfully shown below the HD-FEC threshold using the device.

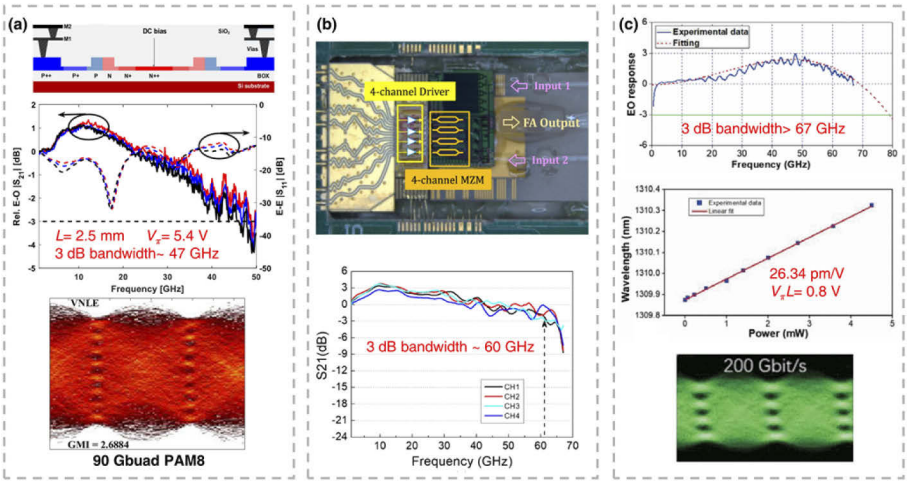

Fig. 7. All silicon modulators. (a) O-band silicon MZM allowing 225 Gbps net rate operation with nonlinear equalization [95], licensed under a Creative Commons Attribution 4.0 License. (b) 4-channel SiP transmitter and EO S_{21} response of SiP modulators. Reprinted with permission from [96]. Copyright 2020, Chinese Laser Press. (c) Silicon microring modulator. Reprinted with permission from [97]. Copyright 2020, IEEE.

To date, silicon modulators not only remain challenging to achieve 100-GHz bandwidth but also suffer from optical loss and nonlinear response owing to the physical limitation of the plasma dispersion effect. Many research teams have attempted to integrate excellent electro-optic materials into a mature silicon photonics platform, such as organic EO material, LN, (silicon-) germanium (Ge) and 2D materials. Heterogeneous integration with silicon photonics is an alternative solution to overcome bandwidth and loss limits that stem from the physics of the plasma dispersion effect [98]. As an alternative solution to overcome the bandwidth and loss limits that stem from the plasma dispersion effect, hybrid Si modulators pave the way to feature the required functionality and convenience for silicon photonics together with efficient EO materials.

Silicon platforms can incorporate organic EO materials to form silicon-organic hybrid (SOH) and plasmonic-organic hybrid (POH) platforms, which combine silicon waveguides and plasmonic nanostructures with organic EO materials as cladding [99]. Generally, SOI waveguides are fabricated using standard CMOS processes, and then the EO organic material is deposited to

Optics EXPRESS

fill the silicon strip-load slot waveguide, in which the optical mode is highly confined in the narrow slot region. To activate the microscopic EO effect, the organic materials need to be poled by heating them close to their glass-transition temperatures T_g while applying an external electric field. The chromophore molecules align with the poling field in this procedure; thus, a non-centrosymmetric orientation is formed [100–102].

To date, SOH modulators have shown advances in ultra-high modulation efficiency (320 Vμm [102]) and low drive voltage (on a scale of a few hundred millivolts). Nevertheless, the bandwidth of the conventional slot-waveguide SOH modulators is limited by the high *RC* time constant (~ 25 GHz [103]), corresponding to the capacitance of the slot and the resistance of the doped Si slabs. Slot waveguides can realize low resistivity by increasing the doping concentration of the conductive slabs, which increases the EO bandwidth but at the cost of optical loss. A novel method to overcome the RC limitation of a conventional SOH modulator is to replace the doped Si slabs with $BaTiO_3$ [104]. $BaTiO_3$ is a high-κ dielectric material that effectively avoids the resistive slab and forms a large coupling capacitor between the optical slot waveguides. As shown Fig. 8(a), the 1-mm-long capacitively coupled SOH modulator features a bandwidth of 76 GHz and a V_π of 1.3 V.

Long-term reliability and stability, including thermal and photo-induced degradation, require further verification of the SOH modulator. The poled film should be operated and stored below T_g to avoid thermal relaxation of the chromophore. Therefore, EO polymers with a high T_g might offer better thermal stability. As shown in Fig. 8(b), EO polymers with an ultra-high T_g of 172 °C were spin-coated onto silicon rib waveguides. The device demonstrated 200 Gbit/s PAM4 modulations with a slight BER increase over a wide temperature range (25–110 °C) [105]. An alternative solution is to replace the poled chromophore molecules with organic EO crystals, which are inherently stable in the photochemical processes. Moreover, the alignment of the organic crystals is stable and independent of the operating temperature [106].

The fundamental difference between the POH and the SOH is that the former uses metal-slot waveguides rather than silicon slot waveguides. In the modulation region of POH, both the optical and microwave signals are guided by the narrow metal slot filled with the EO polymer material. Optical signals work in strongly localized plasmon modes to overcome the diffraction limit of light [107]. Such strong EO interaction and confinement make the POH modulator stand out for its microscale footprint. Owing to their small capacitance as well as small size, SOH modulators generally feature low power consumption and ultra-high bandwidths without requiring terminations. As shown in Fig. 8(c), the POH MZM features a $V_\pi L$ of 60 V μm and bandwidth beyond 70 GHz in a total configuration length of 10 μm [108]. Although SPP waveguides suffer from high propagation loss (0.4 dB/μm [108]), reasonable on-chip optical loss (9 dB for MZM 2.5 dB for optimized ring structure [109]) can be achieved owing to ultra-short phase shifters. The optimized SOH MZM demonstrates great potential for sub-terahertz-range applications with a flat EO frequency greater than 500 GHz. (Fig. 2(e)). As shown in Fig. 8(d), a POH IQ modulator shows energy-efficient high-speed coherent modulation. The modulator was driven by sub-1 V driving electronics to generate a 16 QAM 50 Gbaud (200 Gbit/s) signal with a BER below the SD-FEC limit and an energy consumption of 0.3 fJ/bit.

Several approaches attempt to bond the LN film on top of the SOI chip, thereby, combining CMOS compatibility of silicon photonics with the excellent EO performance of LNOI. In the past decade, unpatterned LN films were bonded to ridge [8,110] or rib [14,61,62] silicon waveguides. A drawback of these hybrid waveguides is the small mode overlap between the optical field and the LN film Γ_{LN}. By reducing the width of the silicon waveguide to 320 nm in the modulation region [61], the guided mode is "extruded" from the silicon waveguide to achieve a larger mode overlap (Γ_{LN} = 81%) with the LN top cladding (Fig. 8(e)). This Si/LN hybrid modulator features an EO bandwidth greater than 106 GHz. However, hybrid waveguides have relatively large optical mode sizes and weak confinement, leading to compromised modulation efficiency. To address

Optics EXPRESS

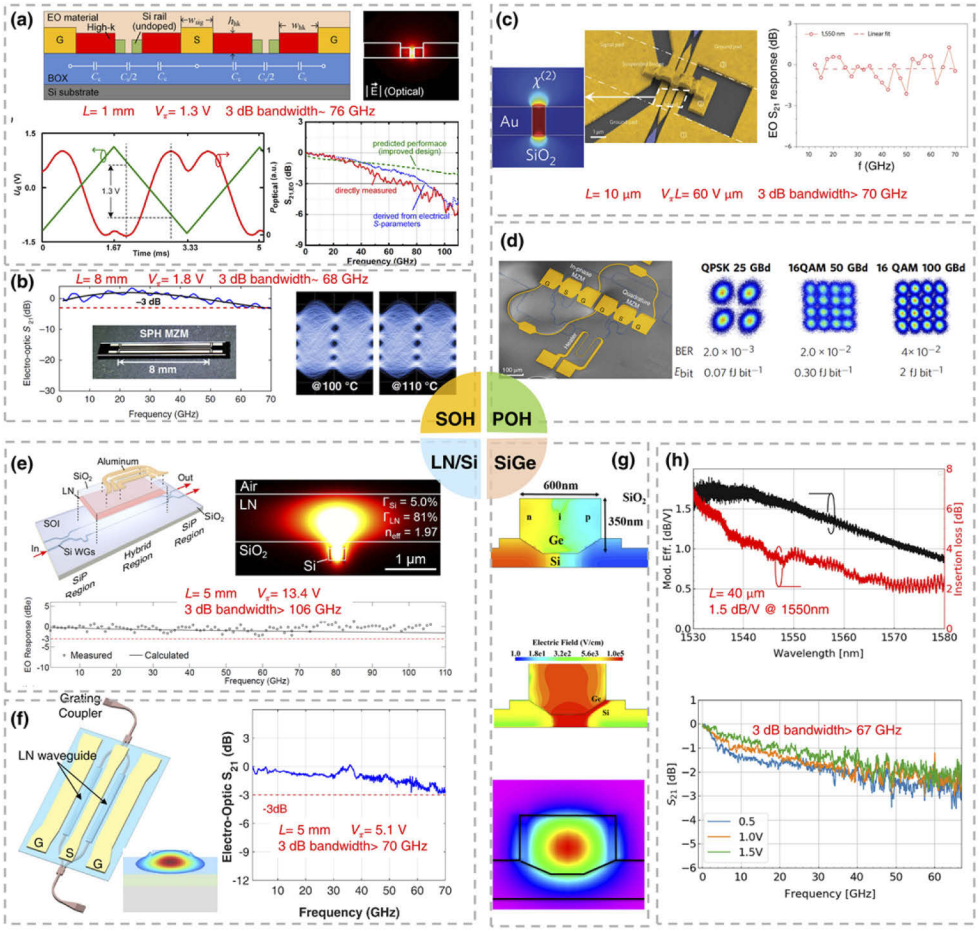

Fig. 8. (a) Capacitivity coupled SOH MZM with high-κ slotlines. Reprinted with permission from [104]. Copyright 2021, Optical Society of America. (b) High-temperature-resistant SOH operating up to 200 Gbit/s [105], licensed under a Creative Commons Attribution 4.0 License. (c) POH MZM with metal–insulator–metal plasmonic slot waveguides. Reprinted by permission from Springer Nature: C. Haffner et al., Nat. Photonics 9(8), 525–528 (2015) [108]. Copyright 2015, Nature Publishing Group. (d) Energy-efficient POH IQ modulator [118], licensed under a Creative Commons Attribution 4.0 License. (e) Si/LN modulator with unpatterned LN film bonded on SOI platform. Reprinted with permission from [61]. Copyright 2018, Optical Society of America. (f) Si/LN modulator with patterned LN film bonded on SOI platform. Reprinted from [45]. Copyright 2019, The Author(s), under exclusive license to Springer Nature Limited. (g) GeSi EAM device integrated on SOI platform. Reprinted with permission from [112]. Copyright 2016, IEEE. (h) Optical and EO performance of the GeSi EAM [117], licensed under a Creative Commons Attribution 4.0 License.

this problem, M. He et al. [45] proposed a two-layer structure in which the upper layer is an etched LN waveguide (Γ_{LN}>90%), and the bottom layer is an SOI circuit containing all passive devices (Fig. 8(f)). In this hybrid structure, vertical adiabatic couplers (VACs) act as "bridges" for light coupling between the silicon and LN waveguides. Highly confined LN waveguides lead to a high modulation efficiency of 2.2 Vcm. For a 5-mm long device, and an EO bandwidth greater than 70 GHz was realized [45].

Optics EXPRESS

The Ge/GeSi-on-Si electro-absorption modulator, an alternative high-bandwidth hybrid Si platform, utilizes an FKE in GeSi or Ge bulk semiconductors [111–114] or QCSE in Ge/GeSi QW [115,116]. The $Ge_{1-x}Si_x$ typically has a wider bandgap energy of FKE EAMs than that of pure Ge, potentially controlling the operation wavelengths. It should note that the composition of Si should keep low to avoid significantly degrading the absorption contrast. Recently, the Ge-on-Si EAM was shown broader optical wavelength (C-band) with the submicron-width optical waveguides [114]. The FKE GeSi modulators are promising for realizing high bandwidth (> 50 GHz [112]) owing to the low junction capacitance in the lateral p-i-n diode Ge islands, which can be fabricated by selectively growing Ge [112] or butt-coupling vertical GeSi [111]. The aim is to form highly confined optical waveguides having an effective overlap with the electrical field (see Fig. 8(g)). Recently, a differential drive GeSi IQ modulator with an EO bandwidth of 67 GHz and modulation efficiency of 1.5 dB/V was demonstrated (Fig. 8(h)). With this advanced GeSi EAM, 100 Gbaud QPSK, and 50 Gbaud 16 QAM were generated with a BER less than the HD-FEC threshold. The record data rate for the GeSi modulator is 200 Gbit/s [117] for coherent transmission and 60 Gbit/s [116] for IM-DD. The limited extinction ratio (< 10 dB) and large absorption loss (typical 4–8 dB) deteriorate the performance of optical transmission systems.

3.4. Two-dimensional (2D) modulator

In recent years, 2D material, including graphene [119–125], black phosphorous [126], and transition metal dichalcogenides (such as MoS_2 [127]), have attracted tremendous attention for optical modulators. The 2D material can bring competitive advantages to the EO modulators, such as small footprint, intrinsic high modulation speed, broadband optical operation, strong light-matter interaction, and structural compatibility. In this review, we only discuss 2D EO modulators with at least tens of gigahertz bandwidth. Graphene is a zero bandgap semiconductor with high electrons mobility. With externally applied voltage to a graphene-insulator-Si or graphene-insulator-graphene capacitor, the surface carrier concentration change rapidly enables absorptive modulation in the optical waveguides. In this process, the Fermi energy significantly shifts to modify interband optical transition in graphene. As shown in Fig. 9(a), a representative work has demonstrated a monolayer graphene-Al_2O_3-Si waveguide (doped) with a broad optical bandwidth (1.35–1.6 mm), small device footprint (25 mm^2) but a limited bandwidth (1.2 GHz) [128]. In 2015, the first high-speed graphene-based modulator was demonstrated [119]. The silicon nitride waveguides guided the light in the ring and the graphene-insulator-graphene capacitor covered part of the ring resonator. The compact modulator features a 15 dB extinction ratio over 10 V and 30 GHz EO bandwidth [Fig. 9(b)]. Graphene-insulator-graphene structure allows almost double electro-absorption and electro-refraction effect compared with the single-layer graphene structure. As shown in Fig. 9(c), un-doped silicon acts as the guiding material and a stack of hexagonal boron nitride (hBN)–hafnium oxide (HfO_2)–hBN dielectric acts as a sandwich between the two graphene layers. The sandwich structure brings a carrier density-independent high mobility (30 000 $cm^2\ V^{-1}\ s^{-1}$) and higher modulation efficiency, allowing 40 Gbit/s OOK modulation [129]. To our knowledge, the highest measured EO bandwidth graphene-based modulator is only 39 GHz [129]. Few theoretical research has predicted the bandwidth can reach 120 GHz [130,131]. Moreover, based on the photo-thermoelectric effect, graphene-based photodetectors have demonstrated large bandwidth of > 65 GHz [132–134].

To date, although wafer-level graphene photonic devices have been demonstrated [134], the mature and mass production of graphene devices is not very optimistic. There are kinds of remaining technical problems, such as high-quality graphene transfer, high-quality dielectric film deposition, and wafer-scale production with reliable performance. It is also challenging to realize high mobility, low loss, decent modulation depth, and high modulation efficiency synchronously.

Optics EXPRESS

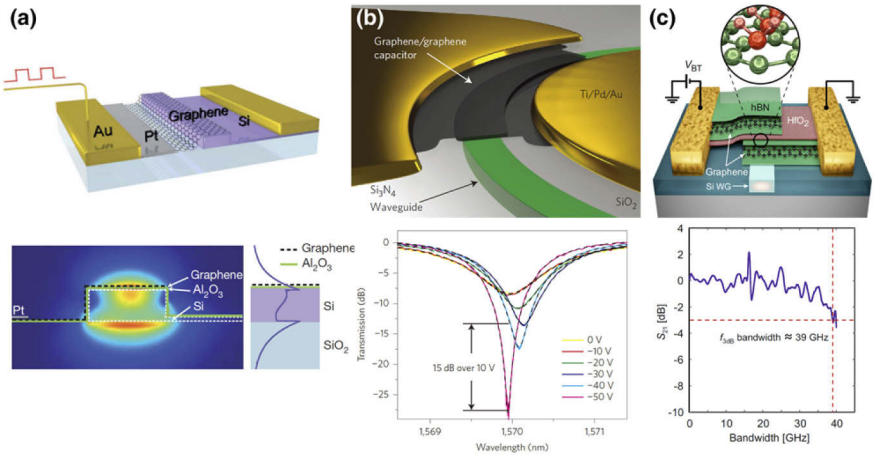

Fig. 9. (a) Monolayer graphene-on-Si waveguide-integrated modulator. Reprinted by permission from Springer Nature: M. Liu et al., Nature 474(7349), 64–67 (2011) [128]. Copyright 2011, Nature Publishing Group, a division of Macmillan Publishers Limited. (b) A graphene-insulator-graphene microring modulator with a modulation efficiency of 15 dB per 10 V. Reprinted by permission from Springer Nature: Christopher T. Phare et al., Nat Photonics 9(8), 511–514 (2015) [119]. Copyright 2015, Nature Publishing Group. (c) A graphene- hBN-HfO_2-hBN-graphene modulator with 39 GHz EO bandwidth [129], licensed under a Creative Commons Attribution 4.0 License.

3.5. *Key performance metrics beyond bandwidth*

Half-wave voltage. V_π is the required voltage to induce π phase change. $V_\pi L$ is a constant and related to the optical and electrodes design. Longer modulation regions result in a lower V_π and lower power consumption, but a smaller bandwidth due to higher microwave loss and accumulation of velocity mismatch. A practical modulator should optimize the length of the electrodes and balance the trade-off between bandwidth and V_π. We use BW/V_π as the figure of merit in this review. Bandwidth-voltage performance has the most significant impact on the EO performance of the modulator, especially in high-baud-rate transmission systems. LNOI, InP, SOH, and POH have shown outstanding bandwidth-voltage performance, which is promising for future single-carrier terabit-per-second transmission.

Insertion loss. In the optical links, device loss and attainable input optical power determine the optical signal-to-noise ratio (SNR) to a large extent. Higher-order modulation formats require higher optical SNR for the increase of the number of bit/symbols. In short-reach interconnect, the optical link budget is tight, requiring low total insertion loss of modulators (on-chip loss and fiber-to-chip coupling loss). On the one hand, POH, SiGe, and graphene-based modulators suffer from high propagation loss, which can be overcome by short modulation length (tens of micrometer). However, low V_π is harder to achieve in such a short length. Propagation loss comes to the primary consideration for future large-scale photonic integration circuits (PIC). On the other hand, low-loss fiber-to-chip couplers are essential and challenge for mode matching between fiber and submicron optical waveguides.

Linearity. Modulators are expected to operate at the linear region, especially for multi-level PAM and high-order QAM. Nonlinear distortion in modulation requires complex nonlinear compensation in the digital signal processing (DSP) process. Moreover, linearity is the key parameter that determines the performance in integrated microwave photonics (MWPs) system. We can characterize the linearity by evaluating the third-order intermodulation (IMD3) spurious-free dynamic range (SFDR) performance. SFDR is defined as the ratio of the maximum signals

Optics EXPRESS

without distortion to the minimum signal above the system noise floor. The schematic of the experimental setup is shown in Fig. 10(a). Applying two fundamental signals with equal amplitude at frequency f_1,f_2 to the EO modulators, IMD3 frequency terms ($2f_1$-f_2 and $2f_2$-f_1) generate in the modulation if linearity exits. Note that IMD3 frequency terms are the dominating distortion components in analog optical links, which are close to the fundamental signal and difficult to filter out. Then the optical signal is detected by a photodetector and sent to the RF spectrum analyzer. After recording the RF output power of the fundamental signal and IMD3, we can obtain the SFDR, third-order input intercept power (IIP3), third-order output intercept power (OIP3), and noise figure (NF) [Fig. 10(b)].

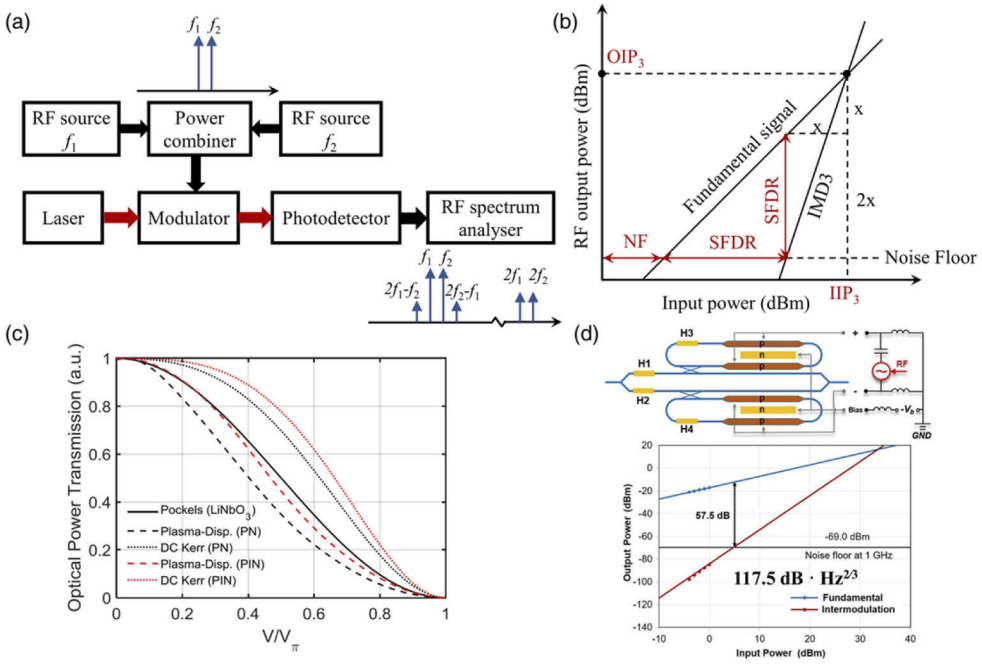

Fig. 10. (a) Experimental setup for measuring the SFDR. (b) RF output power of the fundamental and IMD3 components as a function of RF input power. (c) Simulated MZM transfer functions based on Pockels effect, plasma dispersion and DC Kerr effect. Reprinted with permission from [135]. Copyright 2019, IEEE. (d) Linearized heterogeneously III–V/Si ring-assisted MZM with SFDR of 117.5 dB · $Hz^{2/3}$ at 10 GHz. Reprinted with permission from [136]. Copyright 2016, Optical Society of America.

EO modulators on various material platforms based on different modulation mechanisms, of which is a linear index-voltage relationship, such as the LN modulator that relies on the Pockels effect, while others are intrinsic nonlinear, such as the silicon modulator that relies on plasma dispersion effect (index change~ $\sqrt{V}$) and direct current (DC) Kerr effect (index change~ V^2), and the InP based on QCSE and FKE. The transfer functions of the MZM based on the Pockels effect, plasma dispersion effect, and DC Kerr effect are shown in Fig. 10(c) [135]. MZM based on linear EO effect has an ideal sinusoidal transfer with the maximum SFDR at the quadrature point. Transfer function engineering can be accomplished by device design and biasing for electro-absorption devices [135]. Several schemes for the linearization approach include resonant-assisted MZM [136,137] [Fig. 10(d)], dual-parallel MZM [138,139], cascaded MZM [140] and dual ring [141].

Temperature stability. InP and partly Ge/SiGe modulator utilize QCSE in MQW waveguides. QCSE is a temperature-sensitive effect. As the temperature increases, the bandgap becomes

Optics EXPRESS

narrower and the absorption edge widens. In practice, thermoelectric coolers (TEC) can use for stable operation. Low-temperature-dependent InP-based modulator has been realized by reducing V_π (1.5 V) thus a smaller swing voltage of the driver, which indicates a low EO bandwidth variation of 2 GHz under 25° to 85 °C conditions [76]. Previous investigation of Ge/SiGe MQW, the absorption coefficient spectra redshift with the temperature dependence of ~0.83 nm/°C [142].

4. Conclusion and future outlook

In this review, we summarize different driving electrodes and optical structures that can broaden the EO bandwidth. These schemes are universal and can be adopted on various integrated platforms. With a few promising EO platforms as our focus, we reviewed high-bandwidth modulators on each of them and briefly analyzed their advantages and disadvantages. Inevitable trade-offs were observed among bandwidth, voltage, power consumption, size, and loss. Table 1 presents the state-of-the-art performance for the high-bandwidth modulator in LNOI, InP, Si, and hybrid Si platforms, including 3-dB EO bandwidth, BW/V_π, footprint, loss, and net bit rate.

Table 1. Typical and state-of-the-art performance for the high-bandwidth MZM on various EO platforms. The parentheses conclude the best-reported result.

Platform	Operating principle	3-dB EO bandwidth [GHz]	Record BW/V_π [GHz/V]	Footprint [mm]	Loss [dB/cm]	Record net data rate [Gb/s/λ]
LNOI	Pockels	>67 (110 [44])	80 [68]	5~20	~0.3	700 [57]
InP	QCSK/FK	>67 (80 [61])	53 [77]	~4	~2 (1.5 [77])	333 [73]
Si	Free-carrier dispersion	~40 (60 [97])	<10 [96]	<5	10~30 (2.6 [146])	225 [96]
SOH	Pockels	60 (76 [105])	58 [105]	~1.5	~20 (22 [106])	187 [147]
POH	Pockels	100 (500 [22])	166 [22]	<0.02	~ 500 (400 [108])	200 [148]
LN/Si	Pockels	70 (106 [61])	14 [45]	>5	~1 (0.98 [45])	105 [45]
(Si-)Ge	FK/QCSE	50 (>67 [118])	N.A.	~0.04	1000	133 [149]
Graphene	Interband transition	30 (39 [129])	N.A.	~0.05	300 [120]	50 [124]

LN-based and organic-based modulators operate with the linear Pockels effect, which can offer intrinsically good linearity and reduce the budget for nonlinear compensation in transmission. Particularly, LNOI is superior in the overall performance of ultra-low loss, high bandwidth, low V_π, and demonstrated the highest net data rate. In addition, LNOI has a wide optical operation bandwidth (C + O-band [143]) and temperature stability. However, for a CMOS-level driving voltage (< 1 V), the LNOI modulator requires a modulation length of 1–2 cm, which is difficult to achieve owing to the fixed r_{33} coefficient. Devices are extremely long to be practically adapted to a compact transceiver package, such as QSFP-DD (quad small form-factor pluggable double density). By employing meander TWE and optical waveguides, folded LNOI-based MZMs were found to be effective solutions to reduce the device length while maintaining the overall performance [64,144]. Booming LNOI-based modulators are becoming increasingly popular in the commercial market. Moreover, the demonstration of wafer-level LN photonics integrated circuits [48] makes the platform promising for cost-effective applications.

InP enjoys an ultrafast EO response owing to the QCSK/FK effect, which is beneficial for high EO bandwidth and low driving voltage. The development of high-bandwidth InP modulators is accompanied by optimizing the heterostructure to reduce the series semiconductor resistance.

Optics EXPRESS

Furthermore, the InP platform can support lasers and amplifiers in the monolithic integration with modulators, which is extremely appealing from the perspective of photonic integration.

All Si modulators cost-effectively support a high data rate and are suitable for low-cost commercial deployment with microelectronics. Silicon optical modulators show great promise for applications up to a bandwidth of 100 GHz. When the bandwidth requirement is greater than 100 GHz, Si hybrid modulators have the potential to overcome the bandwidth and loss limitations due to the plasma dispersion effect.

Reportedly, SOH has the highest modulation index (0.032 Vcm [102]) owing to the large Pockels coefficient (r_{33}= 390 pm/V [102]) from organic EO material. The BW/V_π value of the SOH is much higher than that of all the Si modulators. For organic/polymer-based modulators, the long-term thermal and photochemical stability still faces skepticism, although recent advances have demonstrated that they can operate stably at elevated temperatures [105,145]. POH modulators have the highest BW/V_π and the smallest footprint, making them promising for ultra-high bandwidth density and low power consumption. However, POH modulators suffer from high propagation losses. Therefore, the phase shifters must be kept sufficiently short for reasonable on-chip insertion loss. Hybrid LN/Si modulators combine excellent EO performance from LN with silicon circuity. To date, the BW/V_π value of the hybrid LN/Si modulator is lower than that of LNOI owing to the RF loss from the silicon substrate of the current SOI. By employing an SOI wafer with a silicon substrate with high resistance or substrate removal techniques, the BW/V_π of hybrid LN/Si can catch up with the LNOI platform in the future.

For EO modulators with modulation bandwidth approaching or exceeding 100 GHz, it is essential to determine the scheme of the modulated electrode and optical waveguide based on the characteristics of the specific material platforms, sometimes at the cost of increasing the driving voltage. The aforementioned integrated platforms are promising candidates for ultra-wideband optical communications with distinct advantages.

Funding. National Key Research and Development Program of China (2019YFA0705000, 2019YFB1803900); National Natural Science Foundation of China (11690031, 11761131001).

Disclosures. The authors declare that there are no conflicts of interest related to this article.

Data availability. The data that support the findings of this study are available from the corresponding author upon reasonable request.

References

1. Cisco, Cisco Annual Internet Report (2018–2023) White Paper (2020).
2. A. Honardoost, R. Safian, A. Rao, and S. Fathpour, "High-Speed Modeling of Ultracompact Electrooptic Modulators," J. Lightwave Technol. **36**(24), 5893–5902 (2018).
3. J. Witzens, "High-Speed Silicon Photonics Modulators," Proc. IEEE **106**(12), 2158–2182 (2018).
4. G. Sinatkas, T. Christopoulos, O. Tsilipakos, and E. E. Kriezis, "Electro-optic modulation in integrated photonics," J. Appl. Phys. **130**(1), 010901 (2021).
5. G. Ghione, *Semiconductor Devices for High-Speed Optoelectronics* (Cambridge University, 2009).
6. A. Chen and E. Murphy, *Broadband Optical Modulators* (CRC, 2011).
7. G. Li, A. V. Krishnamoorthy, I. Shubin, J. Yao, Y. Luo, H. Thacker, X. Zheng, K. Raj, and J. E. Cunningham, "Ring Resonator Modulators in Silicon for Interchip Photonic Links," IEEE J. Sel. Top. Quantum Electron. **19**(6), 95–113 (2013).
8. L. Chen, Q. Xu, M. G. Wood, and R. M. Reano, "Hybrid silicon and lithium niobate electro-optical ring modulator," Optica **1**(2), 112–118 (2014).
9. H. Yu, D. Q. Ying, M. Pantouvaki, J. Van Campenhout, P. Absil, Y. L. Hao, J. Y. Yang, and X. Q. Jiang, "Trade-off between optical modulation amplitude and modulation bandwidth of silicon micro-ring modulators," Opt. Express **22**(12), 15178–15189 (2014).
10. H. Shoman, H. Jayatilleka, A. H. K. Park, A. Mistry, N. A. F. Jaeger, S. Shekhar, and L. Chrostowski, "Compact wavelength- and bandwidth-tunable microring modulator," Opt. Express **27**(19), 26661–26675 (2019).
11. Y. Tong, Z. Hu, X. Wu, S. Liu, L. Chang, A. Netherton, C. Chan, J. E. Bowers, and H. K. Tsang, "An Experimental Demonstration of 160-Gbit/s PAM-4 using a Silicon Micro-Ring Modulator," IEEE Photonics Technol. Lett. **32**(2), 125–128 (2020).

Optics EXPRESS

12. Y. Y. Meisam Bahadori, Ahmed E. Hassanien, Lynford L. Goddard, and Gong Songbin, "Ultra-efficient and fully isotropic monolithic microring modulators in a thin-film lithium niobate photonics platform," Opt. Express **28**(20), 29644–29661 (2020).
13. A. N. R. Ahmed, S. Shi, A. J. Mercante, and D. W. Prather, "High-performance racetrack resonator in silicon nitride - thin film lithium niobate hybrid platform," Opt. Express **27**(21), 30741–30751 (2019).
14. L. Chen, J. Chen, J. Nagy, and R. M. Reano, "Highly linear ring modulator from hybrid silicon and lithium niobate," Opt. Express **23**(10), 13255–13264 (2015).
15. R. Yang, L. Zhou, H. Zhu, and J. Chen, "Low-voltage high-speed coupling modulation in silicon racetrack ring resonators," Opt. Express **23**(22), 28993–29003 (2015).
16. E. Timurdogan, C. M. Sorace-Agaskar, J. Sun, E. Shah Hosseini, A. Biberman, and M. R. Watts, "An ultralow power athermal silicon modulator," Nat. Commun. **5**(1), 4008 (2014).
17. M. Xu, M. He, Y. Zhu, L. Liu, L. Chen, S. Yu, and X. Cai, "Integrated thin film lithium niobate Fabry–Perot modulator," Chin. Opt. Lett. **19**(6), 060003 (2021).
18. M. Li, J. Ling, Y. He, U. A. Javid, S. Xue, and Q. Lin, "Lithium niobate photonic-crystal electro-optic modulator," Nat. Commun. **11**(1), 4123 (2020).
19. K. Nozaki, A. Shakoor, S. Matsuo, T. Fujii, K. Takeda, A. Shinya, E. Kuramochi, and M. Notomi, "Ultralow-energy electro-absorption modulator consisting of InGaAsP-embedded photonic-crystal waveguide," APL Photonics **2**(5), 056105 (2017).
20. E. Li, B. Zhou, Y. Bo, and A. X. Wang, "High-Speed Femto-Joule per Bit Silicon-Conductive Oxide Nanocavity Modulator," J. Lightwave Technol. **39**(1), 178–185 (2021).
21. D. Pohl, A. Messner, F. Kaufmann, M. R. Escalé, J. Holzer, J. Leuthold, and R. Grange, "100-GBd Waveguide Bragg Grating Modulator in Thin-Film Lithium Niobate," IEEE Photonics Technol. Lett. **33**(2), 85–88 (2021).
22. M. Burla, C. Hoessbacher, W. Heni, C. Haffner, Y. Fedoryshyn, D. Werner, T. Watanabe, H. Massler, D. L. Elder, L. R. Dalton, and J. Leuthold, "500 GHz plasmonic Mach-Zehnder modulator enabling sub-THz microwave photonics," APL Photonics **4**(5), 056106 (2019).
23. Z. Jingjing, S. Alexandrou, and T. Y. Hsiang, "Attenuation characteristics of coplanar waveguides at subterahertz frequencies," IEEE Trans. Microwave Theory Tech. **53**(11), 3281–3287 (2005).
24. Rainee Simons, *Coplanar Waveguide Circuits, Components, and Systems* (John Wiley & Sons, 2001), pp. 203–236.
25. R.-Y. Yang, C.-Y. Hung, Y.-K. Su, M.-H. Weng, and H.-W. Wu, "Loss characteristics of silicon substrate with different resistivities," Microw. Opt. Technol. Lett. **48**(9), 1773–1776 (2006).
26. R. G. Geyer and J. Krupka, "Microwave dielectric properties of anisotropic materials at cryogenic temperatures," IEEE Trans. Instrum. Meas. **44**(2), 329–331 (1995).
27. M. Kusunoki, M. Inadomaru, S. Ohshima, K. Aizawa, M. Mukaida, M. Lorenz, and H. Hochmuth, "Dielectric loss tangent of sapphire single crystal produced by edge-defined film-fed growth method," Physica C: Superconductivity **377**(3), 313–318 (2002).
28. M. F. Li, L. Wang, X. Li, X. Xiao, and S. H. Yu, "Silicon intensity Mach-Zehnder modulator for single lane 100 Gb/s applications," Photonics Res. **6**(2), 109–116 (2018).
29. J. Shin, S. R. Sakamoto, and N. Dagli, "Conductor Loss of Capacitively Loaded Slow Wave Electrodes for High-Speed Photonic Devices," J. Lightwave Technol. **29**(1), 48–52 (2011).
30. S. JaeHyuk, C. Ozturk, S. R. Sakamoto, Y. J. Chiu, and N. Dagli, "Novel T-rail electrodes for substrate removed low-voltage high-speed GaAs/AlGaAs electrooptic modulators," IEEE Trans. Microwave Theory Tech. **53**(2), 636–643 (2005).
31. R. Ding, Y. Liu, Y. Ma, Y. Yang, Q. Li, A. E. Lim, G. Lo, K. Bergman, T. Baehr-Jones, and M. Hochberg, "High-Speed Silicon Modulator With Slow-Wave Electrodes and Fully Independent Differential Drive," J. Lightwave Technol. **32**(12), 2240–2247 (2014).
32. P. Kharel, C. Reimer, K. Luke, L. He, and M. Zhang, "Breaking voltage–bandwidth limits in integrated lithium niobate modulators using micro-structured electrodes," Optica **8**(3), 357–363 (2021).
33. X. Liu, B. Xiong, C. Sun, J. Wang, Z. Hao, L. Wang, Y. Han, H. Li, J. Yu, and Y. Luo, "Wideband thin-film lithium niobate modulator with low half-wave-voltage length product," Chin. Opt. Lett. **19**(6), 060016 (2021).
34. A. Samani, E. El-Fiky, M. Morsy-Osman, R. Li, D. Patel, T. Hoang, M. Jacques, M. Chagnon, N. Abadía, and D. V. Plant, "Silicon Photonic Mach–Zehnder Modulator Architectures for on Chip PAM-4 Signal Generation," J. Lightwave Technol. **37**(13), 2989–2999 (2019).
35. M. Jacques, A. Samani, E. El-Fiky, and D. V. Plant, "Silicon Photonic MZM Architectures for 200G per Lambda IM/DD Transmission," in *Optical Fiber Communication Conference (OFC) 2021, OSA Technical Digest* (Optical Society of America, 2021), W7F.1.
36. M. Jacques, Z. Xing, A. Samani, E. El-Fiky, X. Li, M. Xiang, S. Lessard, and D. V. Plant, "240 Gbit/s Silicon Photonic Mach-Zehnder Modulator Enabled by Two 2.3-Vpp Drivers," J. Lightwave Technol. **38**, 1 (2020).
37. L. Breyne, H. Ramon, K. Van Gasse, M. Verplaetse, J. Lambrecht, M. Vanhoecke, J. Van Campenhout, G. Roelkens, P. Ossieur, X. Yin, and J. Bauwelinck, "50 GBd PAM4 transmitter with a 55 nm SiGe BiCMOS driver and silicon photonic segmented MZM," Opt. Express **28**(16), 23950–23960 (2020).
38. M. Vanhoecke, A. Aimone, N. Argyris, S. Dris, R. Vaernewyck, K. Verheyen, M. Gruner, G. Fiol, D. Apostolopoulos, H. Avramopoulos, G. Torfs, X. Yin, and J. Bauwelinck, "Segmented Optical Transmitter Comprising a CMOS

Optics EXPRESS

Driver Array and an InP IQ-MZM for Advanced Modulation Formats," J. Lightwave Technol. **35**(4), 862–867 (2017).
39. E. H. Turner, "High-Frequency Electro-Optic Coefficients of Lithium Niobate," Appl. Phys. Lett. **8**, 303 (1966).
40. D. J. Gettemy, W. C. Harker, G. Lindholm, and N. P. Barnes, "Some optical properties of KTP, LiIO/sub 3/, and LiNbO/sub 3," IEEE J. Quantum Electron. **24**(11), 2231–2237 (1988).
41. D. N. Nikogosyan, *Nonlinear optical crystals: a complete survey* (Springer Science & Business Media, 2006).
42. E. L. Wooten, K. M. Kissa, A. Yi-Yan, E. J. Murphy, D. A. Lafaw, P. F. Hallemeier, D. Maack, D. V. Attanasio, D. J. Fritz, G. J. McBrien, and D. E. Bossi, "A review of lithium niobate modulators for fiber-optic communications systems," IEEE J. Sel. Top. Quantum Electron. **6**(1), 69–82 (2000).
43. M. Zhang, C. Wang, R. Cheng, A. Shams-Ansari, and M. Lončar, "Monolithic ultra-high-Q lithium niobate microring resonator," Optica **4**(12), 1536–1537 (2017).
44. C. Wang, M. Zhang, X. Chen, M. Bertrand, A. Shams-Ansari, S. Chandrasekhar, P. Winzer, and M. Lončar, "Integrated lithium niobate electro-optic modulators operating at CMOS-compatible voltages," Nature **562**(7725), 101–104 (2018).
45. M. He, M. Xu, Y. Ren, J. Jian, Z. Ruan, Y. Xu, S. Gao, S. Sun, X. Wen, L. Zhou, L. Liu, C. Guo, H. Chen, S. Yu, L. Liu, and X. Cai, "High-performance hybrid silicon and lithium niobate Mach–Zehnder modulators for 100 Gbit s−1 and beyond," Nat. Photonics **13**(5), 359–364 (2019).
46. J. Ling, Y. He, R. Luo, M. Li, H. Liang, and Q. Lin, "Athermal lithium niobate microresonator," Opt. Express **28**(15), 21682–21691 (2020).
47. C. Wang, M. Zhang, B. Stern, M. Lipson, and M. Loncar, "Nanophotonic lithium niobate electro-optic modulators," Opt. Express **26**(2), 1547–1555 (2018).
48. K. Luke, P. Kharel, C. Reimer, L. He, M. Loncar, and M. Zhang, "Wafer-scale low-loss lithium niobate photonic integrated circuits," Opt. Express **28**(17), 24452–24458 (2020).
49. Y. Liu, H. Li, J. Liu, S. Tan, Q. Lu, and W. Guo, "Low Vπ thin-film lithium niobate modulator fabricated with photolithography," Opt. Express **29**(5), 6320–6329 (2021).
50. M. Wang, R. Wu, J. Lin, J. Zhang, Z. Fang, Z. Chai, and Y. Cheng, "Chemo-mechanical polish lithography: A pathway to low loss large-scale photonic integration on lithium niobate on insulator," Quantum Engineering **1**(1), e9 (2019).
51. B. Desiatov, A. Shams-Ansari, M. Zhang, C. Wang, and M. Lončar, "Ultra-low-loss integrated visible photonics using thin-film lithium niobate," Optica **6**(3), 380–384 (2019).
52. M. Xu, M. He, H. Zhang, J. Jian, Y. Pan, X. Liu, L. Chen, X. Meng, H. Chen, Z. Li, X. Xiao, S. Yu, S. Yu, and X. Cai, "High-performance coherent optical modulators based on thin-film lithium niobate platform," Nat. Commun. **11**(1), 3911 (2020).
53. C. R. Prashanta Kharel, Kevin Luke, Lingyan He, and Mian Zhang, "Breaking voltage-bandwidth limits in integrated lithium niobate modulators using micro-structured electrodes," arXiv:2011.13422 (2020).
54. X. Wang, P. O. Weigel, J. Zhao, M. Ruesing, and S. Mookherjea, "Achieving beyond-100-GHz large-signal modulation bandwidth in hybrid silicon photonics Mach Zehnder modulators using thin film lithium niobate," APL Photonics **4**(9), 096101 (2019).
55. Y. Zhang, M. Xu, H. Zhang, M. Li, J. Jian, M. He, L. Chen, L. Wang, X. Cai, X. Xi, and S. Yu, "220 Gbit/s optical PAM4 modulation based on lithium niobate on insulator modulator," *45th European Conference on Optical Communication* (ECOC 2019) (2019).
56. X. Chen, G. Raybon, D. Che, J. Cho, and K. W. Kim, "Transmission of 200-GBaud PDM Probabilistically Shaped 64-QAM Signals Modulated via a 100-GHz Thin-film LiNbO3 I/Q Modulator," in *Optical Fiber Communication Conference (OFC) 2021, OSA Technical Digest* (Optical Society of America, 2021), F3C.5.
57. X. Chen, J. Cho, G. Raybon, D. Che, K. W. Kim, E. Burrows, P. Kharel, C. Reimer, K. Luke, L. He, and M. Zhang, "Single-Wavelength and Single-Photodiode 700 Gb/s Entropy-Loaded PS-256-QAM and 200-GBaud PS-PAM-16 Transmission over 10-km SMF," in *2020 European Conference on Optical Communications (ECOC)*, 2020), 1–4.
58. J. Chiles and S. Fathpour, "Mid-infrared integrated waveguide modulators based on silicon-on-lithium-niobate photonics," Optica **1**(5), 350–355 (2014).
59. A. Rao, A. Patil, J. Chiles, M. Malinowski, S. Novak, K. Richardson, P. Rabiei, and S. Fathpour, "Heterogeneous microring and Mach-Zehnder modulators based on lithium niobate and chalcogenide glasses on silicon," Opt. Express **23**(17), 22746–22752 (2015).
60. A. Rao, A. Patil, P. Rabiei, A. Honardoost, R. DeSalvo, A. Paolella, and S. Fathpour, "High-performance and linear thin-film lithium niobate Mach–Zehnder modulators on silicon up to 50 GHz," Opt. Lett. **41**(24), 5700–5703 (2016).
61. P. O. Weigel, J. Zhao, K. Fang, H. Al-Rubaye, D. Trotter, D. Hood, J. Mudrick, C. Dallo, A. T. Pomerene, A. L. Starbuck, C. T. DeRose, A. L. Lentine, G. Rebeiz, and S. Mookherjea, "Bonded thin film lithium niobate modulator on a silicon photonics platform exceeding 100 GHz 3-dB electrical modulation bandwidth," Opt. Express **26**(18), 23728–23739 (2018).
62. N. Boynton, H. Cai, M. Gehl, S. Arterburn, C. Dallo, A. Pomerene, A. Starbuck, D. Hood, D. C. Trotter, T. Friedmann, C. T. DeRose, and A. Lentine, "A heterogeneously integrated silicon photonic/lithium niobate travelling wave electro-optic modulator," Opt. Express **28**(2), 1868–1884 (2020).
63. P. Ying, H. Tan, J. Zhang, M. He, M. Xu, X. Liu, R. Ge, Y. Zhu, C. Liu, and X. Cai, "Low-loss edge-coupling thin-film lithium niobate modulator with an efficient phase shifter," Opt. Lett. **46**(6), 1478–1481 (2021).

Optics EXPRESS

64. J. Hu, C. Li, C. Guo, C. Lu, A. P. T. Lau, P. Chen, and L. Liu, "Folded thin-film lithium niobate modulator based on a poled Mach–Zehnder interferometer structure," Opt. Lett. **46**(12), 2940–2943 (2021).
65. S. Sun, M. He, M. Xu, X. Zhang, Z. Ruan, L. Zhou, L. Liu, L. Liu, S. Yu, and X. Cai, "High-Speed Modulator with Integrated Termination Resistor Based on Hybrid Silicon and Lithium Niobate Platform," J. Lightwave Technol. **39**(4), 1108–1115 (2021).
66. S. Sun, M. He, M. Xu, S. Gao, Z. Chen, X. Zhang, Z. Ruan, X. Wu, L. Zhou, L. Liu, C. Lu, C. Guo, L. Liu, S. Yu, and X. Cai, "Bias-drift-free Mach–Zehnder modulators based on a heterogeneous silicon and lithium niobate platform," Photonics Res. **8**(12), 1958–1963 (2020).
67. M. Xu, W. Chen, M. He, X. Wen, Z. Ruan, J. Xu, L. Chen, L. Liu, S. Yu, and X. Cai, "Michelson interferometer modulator based on hybrid silicon and lithium niobate platform," APL Photonics **4**(10), 100802 (2019).
68. M. Zhang, C. Wang, P. Kharel, D. Zhu, and M. Lončar, "Integrated lithium niobate electro-optic modulators: when performance meets scalability," Optica **8**(5), 652–667 (2021).
69. M. Xu, Y. Zhu, F. Pittalà, J. Tang, M. He, W. C. Ng, J. Wang, Z. Ruan, X. Tang, M. Kuschnerov, L. Liu, S. Yu, B. Zheng, and X. Cai, "Dual-polarization thin-film lithium niobate in-phase quadrature modulators for terabit-per-second transmission," Optica **9**(1), 61–62 (2022).
70. J. P. Salvestrini, L. Guilbert, M. Fontana, M. Abarkan, and S. Gille, "Analysis and Control of the DC Drift in $LiNbO_3$-Based Mach–Zehnder Modulators," J. Lightwave Technol. **29**(10), 1522–1534 (2011).
71. H. Jiang, R. Luo, H. Liang, X. Chen, Y. Chen, and Q. Lin, "Fast response of photorefraction in lithium niobate microresonators," Opt. Lett. **42**(17), 3267–3270 (2017).
72. X. Sun, H. Liang, R. Luo, W. C. Jiang, X.-C. Zhang, and Q. Lin, "Nonlinear optical oscillation dynamics in high-Q lithium niobate microresonators," Opt. Express **25**(12), 13504–13516 (2017).
73. H. Yamazaki, M. Nagatani, H. Wakita, Y. Ogiso, M. Nakamura, M. Ida, H. Nosaka, T. Hashimoto, and Y. Miyamoto, "IMDD Transmission at Net Data Rate of 333 Gb/s Using Over-100-GHz-Bandwidth Analog Multiplexer and Mach–Zehnder Modulator," J. Lightwave Technol. **37**(8), 1772–1778 (2019).
74. J. M. Estarán, H. Mardoyan, F. Jorge, O. Ozolins, A. Udalcovs, A. Konczykowska, M. Riet, B. Duval, V. Nodjiadjim, J. Y. Dupuy, X. Pang, U. Westergren, J. Chen, S. Popov, and S. Bigo, "140/180/204-Gbaud OOK Transceiver for Inter- and Intra-Data Center Connectivity," J. Lightwave Technol. **37**(1), 178–187 (2019).
75. S. Lange, S. Wolf, J. Lutz, L. Altenhain, R. Schmid, R. Kaiser, M. Schell, C. Koos, and S. Randel, "100 GBd Intensity Modulation and Direct Detection With an InP-Based Monolithic DFB Laser Mach–Zehnder Modulator," J. Lightwave Technol. **36**(1), 97–102 (2018).
76. J. Ozaki, Y. Ogiso, T. Jyo, H. Hashizume, S. Kanazawa, Y. Ueda, M. Nagatani, H. Yamazaki, H. Tanobe, and M. Ishikawa, "500-Gb/s/λ Operation of Ultra-low Power and Low-temperature-dependence InP-based High-bandwidth Coherent Driver Modulator," J. Lightwave Technol. **38**(18), 5086–5091 (2020).
77. Y. Ogiso, J. Ozaki, Y. Ueda, H. Wakita, M. Nagatani, H. Yamazaki, M. Nakamura, T. Kobayashi, S. Kanazawa, Y. Hashizume, H. Tanobe, N. Nunoya, M. Ida, Y. Miyamoto, and M. Ishikawa, "80-GHz Bandwidth and 1.5-V Vπ InP-Based IQ Modulator," J. Lightwave Technol. **38**(2), 249–255 (2020).
78. M. Y. S. Sowailem, T. M. Hoang, M. Morsy-Osman, M. Chagnon, M. Qiu, S. Paquet, C. Paquet, I. Woods, Q. Zhuge, O. Liboiron-Ladouceur, and D. V. Plant, "770-Gb/s PDM-32QAM Coherent Transmission Using InP Dual Polarization IQ Modulator," IEEE Photonics Technol. Lett. **29**(5), 442–445 (2017).
79. M. Smit, K. Williams, and J. V. D. Tol, "Past, present, and future of InP-based photonic integration," APL Photonics **4**(5), 050901 (2019).
80. M. Chaciński, U. Westergren, B. Stoltz, L. Thylén, R. Schatz, and S. Hammerfeldt, "Monolithically Integrated 100 GHz DFB-TWEAM," J. Lightwave Technol. **27**(16), 3410–3415 (2009).
81. O. Ozolins, X. Pang, M. I. Olmedo, A. Kakkar, A. Udalcovs, S. Gaiarin, J. R. Navarro, K. M. Engenhardt, T. Asyngier, R. Schatz, J. Li, F. Nordwall, U. Westergren, D. Zibar, S. Popov, and G. Jacobsen, "100 GHz Externally Modulated Laser for Optical Interconnects," J. Lightwave Technol. **35**(6), 1174–1179 (2017).
82. M. Chaciński, U. Westergren, B. Stoltz, R. Driad, R. E. Makon, V. Hurm, and A. G. Steffan, "100 Gb/s ETDM Transmitter Module," IEEE J. Sel. Top. Quantum Electron. **16**(5), 1321–1327 (2010).
83. C. R. Doerr, L. Zhang, P. J. Winzer, J. H. Sinsky, A. L. Adamiecki, N. J. Sauer, and G. Raybon, "Compact High-Speed InP DQPSK Modulator," IEEE Photonics Technol. Lett. **19**(15), 1184–1186 (2007).
84. N. Kikuchi, Y. Shibata, K. Tsuzuki, H. Sanjoh, T. Sato, E. Yamada, T. Ishibashi, and H. Yasaka, "80-Gb/s Low-Driving-Voltage InP DQPSK Modulator With an n-p-i-n Structure," IEEE Photonics Technol. Lett. **21**(12), 787–789 (2009).
85. Y. Ogiso, Y. Ohiso, Y. Shibata, and M. Kohtoku, "[011] waveguide stripe direction n-i-p-n heterostructure InP optical modulator," Electron. Lett. **50**(9), 688–690 (2014).
86. A. Aimone, F. Frey, R. Elschner, I. G. Lopez, G. Fiol, P. Rito, M. Gruner, A. C. Ulusoy, D. Kissinger, J. K. Fischer, C. Schubert, and M. Schell, "DAC-Less 32-GBd PDM-256-QAM Using Low-Power InP IQ Segmented MZM," IEEE Photonics Technol. Lett. **29**(2), 221–223 (2017).
87. M. Schell, G. Fiol, and A. Aimone, "DAC-free Generation of M-QAM Signals with InP Segmented Mach-Zehnder Modulators," in *Optical Fiber Communication Conference, OSA Technical Digest (online)* (Optical Society of America, 2017), W4G.4.
88. G. T. Reed, G. Mashanovich, F. Y. Gardes, and D. J. Thomson, "Silicon optical modulators," Nat. Photonics **4**(8), 518–526 (2010).

Optics EXPRESS

89. P. Dong, L. Chen, and Y. -K. Chen, "High-speed low-voltage single-drive push-pull silicon Mach-Zehnder modulators," Opt. Express **20**(6), 6163–6169 (2012).
90. X. Y. Li, X. Xiao, H. Xu, Z. Y. Li, T. Chu, J. Z. Yu, and Y. D. Yu, "Highly Efficient Silicon Michelson Interferometer Modulators," IEEE Photonics Technol. Lett. **25**(5), 407–409 (2013).
91. J. Wang, L. Zhou, H. Zhu, R. Yang, Y. Zhou, L. Liu, T. Wang, and J. Chen, "Silicon high-speed binary phase-shift keying modulator with a single-drive push-pull high-speed traveling wave electrode," Photonics Res. **3**(3), 58–62 (2015).
92. D. Patel, S. Ghosh, M. Chagnon, A. Samani, V. Veerasubramanian, M. Osman, and D. V. Plant, "Design, analysis, and transmission system performance of a 41 GHz silicon photonic modulator," Opt. Express **23**(11), 14263–14287 (2015).
93. Y. Hinakura, D. Akiyama, H. Ito, and T. Baba, "Silicon Photonic Crystal Modulators for High-Speed Transmission and Wavelength Division Multiplexing," IEEE J. Sel. Top. Quantum Electron. **27**(3), 1–8 (2021).
94. H. Yu and W. Bogaerts, "An Equivalent Circuit Model of the Traveling Wave Electrode for Carrier-Depletion-Based Silicon Optical Modulators," J. Lightwave Technol. **30**(11), 1602–1609 (2012).
95. M. S. Alam, X. Li, M. Jacques, Z. Xing, A. Samani, E. El-Fiky, P.-C. Koh, and D. V. Plant, "Net 220 Gbps/λ IM/DD Transmssion in O-Band and C-Band With Silicon Photonic Traveling-Wave MZM," J. Lightwave Technol. **39**(13), 4270–4278 (2021).
96. H. Zhang, M. Li, Y. Zhang, D. Zhang, Q. Liao, J. He, S. Hu, B. Zhang, L. Wang, X. Xiao, N. Qi, and S. Yu, "800 Gbit/s transmission over 1 km single-mode fiber using a four-channel silicon photonic transmitter," Photonics Res. **8**(11), 1776–1782 (2020).
97. Y. Zhang, H. Zhang, M. Li, P. Feng, L. Wang, X. Xiao, and S. Yu, "200 Gbit/s Optical PAM4 Modulation Based on Silicon Microring Modulator," in *2020 European Conference on Optical Communications (ECOC)*, 2020), 1–4.
98. R. Abdul, H. Artur, W. Benjamin, P. Despoina, K. Bart, V. T. Dries, and B. Roel, "Taking silicon photonics modulators to a higher performance level: state-of-the-art and a review of new technologies," Adv. Photonics **3**(02), 024003 (2021).
99. C. Koos, J. Leuthold, W. Freude, M. Kohl, L. Dalton, W. Bogaerts, A. L. Giesecke, M. Lauermann, A. Melikyan, S. Koeber, S. Wolf, C. Weimann, S. Muehlbrandt, K. Koehnle, J. Pfeifle, W. Hartmann, Y. Kutuvantavida, S. Ummethala, R. Palmer, D. Korn, L. Alloatti, P. C. Schindler, D. L. Elder, T. Wahlbrink, and J. Bolten, "Silicon-Organic Hybrid (SOH) and Plasmonic-Organic Hybrid (POH) Integration," J. Lightwave Technol. **34**(2), 256–268 (2016).
100. L. Alloatti, R. Palmer, S. Diebold, K. P. Pahl, B. Chen, R. Dinu, M. Fournier, J.-M. Fedeli, T. Zwick, W. Freude, C. Koos, and J. Leuthold, "100 GHz silicon–organic hybrid modulator," Light Sci Appl **3**(5), e173 (2014).
101. S. Koeber, R. Palmer, M. Lauermann, W. Heni, D. L. Elder, D. Korn, M. Woessner, L. Alloatti, S. Koenig, P. C. Schindler, H. Yu, W. Bogaerts, L. R. Dalton, W. Freude, J. Leuthold, and C. Koos, "Femtojoule electro-optic modulation using a silicon–organic hybrid device," Light: Sci. Appl. **4**(2), e255 (2015).
102. C. Kieninger, Y. Kutuvantavida, D. L. Elder, S. Wolf, H. Zwickel, M. Blaicher, J. N. Kemal, M. Lauermann, S. Randel, W. Freude, L. R. Dalton, and C. Koos, "Ultra-high electro-optic activity demonstrated in a silicon-organic hybrid modulator," Optica **5**(6), 739–748 (2018).
103. S. Wolf, H. Zwickel, W. Hartmann, M. Lauermann, Y. Kutuvantavida, C. Kieninger, L. Altenhain, R. Schmid, J. Luo, A. K. Y. Jen, S. Randel, W. Freude, and C. Koos, "Silicon-Organic Hybrid (SOH) Mach-Zehnder Modulators for 100 Gbit/s on-off Keying," Sci Rep **8**(1), 2598 (2018).
104. S. Ummethala, J. N. Kemal, A. S. Alam, M. Lauermann, A. Kuzmin, Y. Kutuvantavida, S. H. Nandam, L. Hahn, D. L. Elder, L. R. Dalton, T. Zwick, S. Randel, W. Freude, and C. Koos, "Hybrid electro-optic modulator combining silicon photonic slot waveguides with high-k radio-frequency slotlines," Optica **8**(4), 511–519 (2021).
105. G.-W. Lu, J. Hong, F. Qiu, A. M. Spring, T. Kashino, J. Oshima, M. -A. Ozawa, H. Nawata, and S. Yokoyama, "High-temperature-resistant silicon-polymer hybrid modulator operating at up to 200 Gbit s−1 for energy-efficient datacentres and harsh-environment applications," Nat. Commun. **11**(1), 4224 (2020).
106. D. Korn, M. Jazbinsek, R. Palmer, M. Baier, L. Alloatti, H. Yu, W. Bogaerts, G. Lepage, P. Verheyen, P. Absil, P. Guenter, C. Koos, W. Freude, and J. Leuthold, "Electro-Optic Organic Crystal Silicon High-Speed Modulator," IEEE Photonics J. **6**(2), 1–9 (2014).
107. D. F. P. Pile, T. Ogawa, D. K. Gramotnev, Y. Matsuzaki, K. C. Vernon, K. Yamaguchi, T. Okamoto, M. Haraguchi, and M. Fukui, "Two-dimensionally localized modes of a nanoscale gap plasmon waveguide," Appl. Phys. Lett. **87**(26), 261114 (2005).
108. C. Haffner, W. Heni, Y. Fedoryshyn, J. Niegemann, A. Melikyan, D. L. Elder, B. Baeuerle, Y. Salamin, A. Josten, U. Koch, C. Hoessbacher, F. Ducry, L. Juchli, A. Emboras, D. Hillerkuss, M. Kohl, L. R. Dalton, C. Hafner, and J. Leuthold, "All-plasmonic Mach–Zehnder modulator enabling optical high-speed communication at the microscale," Nat. Photonics **9**(8), 525–528 (2015).
109. C. Haffner, D. Chelladurai, Y. Fedoryshyn, A. Josten, B. Baeuerle, W. Heni, T. Watanabe, T. Cui, B. Cheng, S. Saha, D. L. Elder, L. R. Dalton, A. Boltasseva, V. M. Shalaev, N. Kinsey, and J. Leuthold, "Low-loss plasmon-assisted electro-optic modulator," Nature **556**(7702), 483–486 (2018).
110. Y. S. Lee, G.-D. Kim, W.-J. Kim, S.-S. Lee, W.-G. Lee, and W. H. Steier, "Hybrid Si-LiNbO3 microring electro-optically tunable resonators for active photonic devices," Opt. Lett. **36**(7), 1119–1121 (2011).

Optics EXPRESS

111. D. Feng, W. Qian, H. Liang, C. C. Kung, Z. Zhou, Z. Li, J. S. Levy, R. Shafiiha, J. Fong, B. J. Luff, and M. Asghari, "High-Speed GeSi Electroabsorption Modulator on the SOI Waveguide Platform," IEEE J. Sel. Top. Quantum Electron. **19**(6), 64–73 (2013).
112. S. A. Srinivasan, M. Pantouvaki, S. Gupta, H. T. Chen, P. Verheyen, G. Lepage, G. Roelkens, K. Saraswat, D. V. Thourhout, P. Absil, and J. V. Campenhout, "56 Gb/s Germanium Waveguide Electro-Absorption Modulator," J. Lightwave Technol. **34**(2), 419–424 (2016).
113. Y. Tong, Q. Zhang, X. Wu, C.-W. Chow, C. Shu, and H. K. Tsang, "Integrated germanium-on-silicon Franz–Keldysh vector modulator used with a Kramers–Kronig receiver," Opt. Lett. **43**(18), 4333–4336 (2018).
114. J. Fujikata, M. Noguchi, K. Kawashita, R. Katamawari, S. Takahashi, M. Nishimura, H. Ono, D. Shimura, H. Takahashi, H. Yaegashi, T. Nakamura, and Y. Ishikawa, "High-speed Ge/Si electro-absorption optical modulator in C-band operation wavelengths," Opt. Express **28**(22), 33123–33134 (2020).
115. C. Porret, S. A. Srinivasan, S. Balakrishnan, P. Verheyen, P. Favia, H. Bender, P. Ong, R. Loo, J. V. Campenhout, and M. Pantouvaki, "O-Band GeSi Quantum-Confined Stark Effect Electro-Absorption Modulator Integrated in a 220 nm Silicon Photonics Platform," in *2020 IEEE Symposium on VLSI Technology*, 2020), 1–2.
116. S. A. Srinivasan, C. Porret, S. Balakrishnan, Y. Ban, R. Loo, P. Verheyen, J. V. Campenhout, and M. Pantouvaki, "60Gb/s waveguide-coupled O-band GeSi quantum-confined Stark effect electro-absorption modulator," in *2021 Optical Fiber Communications Conference and Exhibition (OFC)*, 2021), 1–3.
117. A. Melikyan, N. Kaneda, K. Kim, Y. Baeyens, and P. Dong, "Differential Drive I/Q Modulator Based on Silicon Photonic Electro-Absorption Modulators," J. Lightwave Technol. **38**, 2872–2876 (2020).
118. W. Heni, Y. Fedoryshyn, B. Baeuerle, A. Josten, C. B. Hoessbacher, A. Messner, C. Haffner, T. Watanabe, Y. Salamin, U. Koch, D. L. Elder, L. R. Dalton, and J. Leuthold, "Plasmonic IQ modulators with attojoule per bit electrical energy consumption," Nat. Commun. **10**(1), 1694 (2019).
119. C. T. Phare, Y. H. D. Lee, J. Cardenas, and M. Lipson, "Graphene electro-optic modulator with 30 GHz bandwidth," Nat Photonics **9**(8), 511–514 (2015).
120. H. Dalir, Y. Xia, Y. Wang, and X. Zhang, "Athermal Broadband Graphene Optical Modulator with 35 GHz Speed," ACS Photonics **3**(9), 1564–1568 (2016).
121. Y. Hu, M. Pantouvaki, J. Van Campenhout, S. Brems, I. Asselberghs, C. Huyghebaert, P. Absil, and D. Van Thourhout, "Broadband 10 Gb/s operation of graphene electro-absorption modulator on silicon," Laser Photon. Rev. **10**(2), 307–316 (2016).
122. V. Sorianello, M. Midrio, G. Contestabile, I. Asselberghs, J. Van Campenhout, C. Huyghebaert, I. Goykhman, A. K. Ott, A. C. Ferrari, and M. Romagnoli, "Graphene–silicon phase modulators with gigahertz bandwidth," Nat. Photonics **12**(1), 40–44 (2018).
123. Q. Ma, G. Ren, A. Mitchell, and J. Z. Ou, "Recent advances on hybrid integration of 2D materials on integrated optics platforms," Nanophotonics **9**(8), 2191–2214 (2020).
124. V. Sorianello, G. Contestabile, and M. Romagnoli, "Graphene on Silicon Modulators," J. Lightwave Technol. **38**(10), 2782–2789 (2020).
125. D. Mao, C. Cheng, F. Wang, Y. Xiao, T. Li, L. Chang, A. Soman, T. Kananen, X. Zhang, M. Krainak, P. Dong, and T. Gu, "Device Architectures for Low Voltage and Ultrafast Graphene Integrated Phase Modulators," IEEE J. Sel. Top. Quantum Electron. **27**(2), 1–9 (2021).
126. R. Peng, K. Khaliji, N. Youngblood, R. Grassi, T. Low, and M. Li, "Midinfrared Electro-optic Modulation in Few-Layer Black Phosphorus," Nano Lett. **17**(10), 6315–6320 (2017).
127. B. Li, S. Zu, J. Zhou, Q. Jiang, B. Du, H. Shan, Y. Luo, Z. Liu, X. Zhu, and Z. Fang, "Single-Nanoparticle Plasmonic Electro-optic Modulator Based on MoS2 Monolayers," ACS Nano **11**(10), 9720–9727 (2017).
128. M. Liu, X. Yin, E. Ulin-Avila, B. Geng, T. Zentgraf, L. Ju, F. Wang, and X. Zhang, "A graphene-based broadband optical modulator," Nature **474**(7349), 64–67 (2011).
129. H. Agarwal, B. Terrés, L. Orsini, A. Montanaro, V. Sorianello, M. Pantouvaki, K. Watanabe, T. Taniguchi, D. V. Thourhout, M. Romagnoli, and F. H. L. Koppens, "2D-3D integration of hexagonal boron nitride and a high-κ dielectric for ultrafast graphene-based electro-absorption modulators," Nat. Commun. **12**(1), 1070 (2021).
130. S. Ye, F. Yuan, X. Zou, M. K. Shah, R. Lu, and Y. Liu, "High-Speed Optical Phase Modulator Based on Graphene-Silicon Waveguide," IEEE J. Sel. Top. Quantum Electron. **23**(1), 76–80 (2017).
131. S. J. Koester and M. Li, "High-speed waveguide-coupled graphene-on-graphene optical modulators," Appl. Phys. Lett. **100**(17), 171107 (2012).
132. Y. Wang, X. Li, Z. Jiang, L. Tong, W. Deng, X. Gao, X. Huang, H. Zhou, Y. Yu, L. Ye, X. Xiao, and X. Zhang, "Ultrahigh-speed graphene-based optical coherent receiver," Nat. Commun. **12**(1), 5076 (2021).
133. S. Marconi, M. A. Giambra, A. Montanaro, V. Mišeikis, S. Soresi, S. Tirelli, P. Galli, F. Buchali, W. Templ, C. Coletti, V. Sorianello, and M. Romagnoli, "Photo thermal effect graphene detector featuring 105 Gbit s−1 NRZ and 120 Gbit s−1 PAM4 direct detection," Nat. Commun. **12**(1), 806 (2021).
134. M. A. Giambra, V. Mišeikis, S. Pezzini, S. Marconi, A. Montanaro, F. Fabbri, V. Sorianello, A. C. Ferrari, C. Coletti, and M. Romagnoli, "Wafer-Scale Integration of Graphene-Based Photonic Devices," ACS Nano **15**(2), 3171–3187 (2021).
135. C. G. Bottenfield, V. A. Thomas, and S. E. Ralph, "Silicon Photonic Modulator Linearity and Optimization for Microwave Photonic Links," IEEE J. Sel. Top. Quantum Electron. **25**(5), 1–10 (2019).

Optics EXPRESS

136. C. Zhang, P. A. Morton, J. B. Khurgin, J. D. Peters, and J. E. Bowers, "Ultralinear heterogeneously integrated ring-assisted Mach–Zehnder interferometer modulator on silicon," Optica **3**(12), 1483–1488 (2016).
137. S. Chen, G. Zhou, L. Zhou, L. Lu, and J. Chen, "High-Linearity Fano Resonance Modulator Using a Microring-Assisted Mach–Zehnder Structure," J. Lightwave Technol. **38**(13), 3395–3403 (2020).
138. Q. Zhang, H. Yu, P. Xia, Z. Fu, X. Wang, and J. Yang, "High linearity silicon modulator capable of actively compensating input distortion," Opt. Lett. **45**(13), 3785–3788 (2020).
139. Y. Yamaguchi, A. Kanno, N. Yamamoto, T. Kawanishi, and H. Nakajima, "Linearized LiNbO3 Modulator with Dual Mach-Zehnder Interferometer and Branched Asymmetric CPW Electrode," in *2017 European Conference on Optical Communication (ECOC)*, 2017), 1–3.
140. Q. Zhang, H. Yu, L. Wang, P. Xia, Q. Cheng, Z. Fu, X. Wang, and J. Yang, "Silicon dual-series Mach-Zehnder modulator with high linearity," Opt. Lett. **44**(23), 5655–5658 (2019).
141. A. Hosseinzadeh and C. T. Middlebrook, "Highly linear dual ring resonator modulator for wide bandwidth microwave photonic links," Opt. Express **24**(24), 27268–27279 (2016).
142. Y. H. Kuo, Y. K. Lee, Y. Ge, S. Ren, J. E. Roth, T. I. Kamins, D. A. B. Miller, and J. S. Harris, "Quantum-Confined Stark Effect in Ge/SiGe Quantum Wells on Si for Optical Modulators," IEEE J. Sel. Top. Quantum Electron. **12**(6), 1503–1513 (2006).
143. S. Sun, M. He, S. Yu, and X. Cai, "Hybrid Silicon and Lithium Niobate Mach-Zehnder Modulators with High Bandwidth Operating at C-band and O-band," in *Conference on Lasers and Electro-Optics, OSA Technical Digest* (Optical Society of America, 2020), STh1F.4.
144. S. Sun, M. Xu, M. He, S. Gao, X. Zhang, L. Zhou, L. Liu, S. Yu, and X. Cai, "Folded Heterogeneous Silicon and Lithium Niobate Mach–Zehnder Modulators with Low Drive Voltage," Micromachines **12**(7), 823 (2021).
145. C. Kieninger, Y. Kutuvantavida, H. Miura, J. N. Kemal, H. Zwickel, F. Qiu, M. Lauermann, W. Freude, S. Randel, S. Yokoyama, and C. Koos, "Demonstration of long-term thermally stable silicon-organic hybrid modulators at 85 °C," Opt. Express **26**(21), 27955–27964 (2018).
146. K. Goi, K. Ogawa, Y. T. Tan, V. Dixit, S. T. Lim, C. E. Png, T.-Y. Liow, X. Tu, G.-Q. Lo, and D.-L. Kwong, "Silicon Mach-Zehnder modulator using low-loss phase shifter with bottom PN junction formed by restricted-depth doping," IEICE Electronics Express **10**(17), 20130552 (2013).
147. C. Kieninger, C. Füllner, H. Zwickel, Y. Kutuvantavida, J. N. Kemal, C. Eschenbaum, D. L. Elder, L. R. Dalton, W. Freude, S. Randel, and C. Koos, "Silicon-organic hybrid (SOH) Mach-Zehnder modulators for 100 GBd PAM4 signaling with sub-1 dB phase-shifter loss," Opt. Express **28**(17), 24693–24707 (2020).
148. W. Heni, B. Baeuerle, H. Mardoyan, F. Jorge, J. M. Estaran, A. Konczykowska, M. Riet, B. Duval, V. Nodjiadjim, M. Goix, J. Dupuy, M. Destraz, C. Hoessbacher, Y. Fedoryshyn, H. Xu, D. L. Elder, L. R. Dalton, J. Renaudier, and J. Leuthold, "Ultra-High-Speed 2:1 Digital Selector and Plasmonic Modulator IM/DD Transmitter Operating at 222 GBaud for Intra-Datacenter Applications," J. Lightwave Technol. **38**(9), 2734–2739 (2020).
149. F. Yang, Y. Zhu, L. Zhang, X. Ruan, Y. Li, and F. Zhang, "GeSi EAM-Based 160 Gb/s Nyquist Half-Cycle Subcarrier Modulation Transmission," IEEE Photonics Technol. Lett. **32**(5), 243–246 (2020).